Adhityo Wicaksono

The locomotive behaviours of the tree-climbing fish, *Periophthalmus variabilis*: a cross-disciplinary approach to bioinspired design

Åbo Akademi University

Adhityo Wicaksono

Born 1989 in Jakarta, Indonesia

Previous studies and degrees

MSc in Plant Breeding, in Universitas Gadjah Mada in 2015

BSc in Biology, Institut Teknologi Bandung in 2011

The locomotive behaviours of the tree-climbing fish, *Periophthalmus variabilis*: a cross-disciplinary approach to bioinspired design

Adhityo Wicaksono

Laboratory of Natural Materials Technology
Centre for Functional Materials at Biological Interfaces (FunMat)
Faculty of Science and Engineering
Åbo Akademi University
Åbo/Turku, Finland
2022

Supervisor

Dr. Parvez Alam, CEng, FIMechE, FIMMM, FRSB
School of Engineering, The University of Edinburgh, United Kingdom

Professor Martti Toivakka
Åbo Akademi University, Turku, Finland

Pre-examiners

Assistant Professor Sandy Kawano
Department of Biological Sciences
George Washington University, Washington, United States

and

Assistant Professor Valentina di Santo
Department of Zoology
Stockholm University, Stockholm, Sweden

Opponent for public defence

Assistant Professor Sandy Kawano
Department of Biological Sciences
George Washington University, Washington, United States

ISBN 978-952-12-4134-5 (print)
ISBN 978-952-12-4135-2 (digital)
Painosalama Oy, Turku, Finland, 2022

To all my family

Those who know me by blood or by fate…

This dissertation is a proof that you don't have to fly to the outer space to find aliens. Take your friends to walk with you, and you'll find it in unexpected places.

Behold… this is a story of fishes who are born to defy gravity and common sense!

Acknowledgements

The work of thesis has been carried out at the Laboratory of Natural Materials Technology (formerly Laboratory of Paper Coating and Converting) between 2016 and 2019. The molecular analysis of DNA barcoding was performed in Turku Centre for Biotechnology, University of Turku and Åbo Akademi University, and some analytical works and field preparation provided by Universitas Gadjah Mada, Indonesia. The first year of the research was financially supported by the Centre for International Mobility (CIMO) scholarship (grant no. TM-15-9783).

I wish to express my greatest gratitude to my primary supervisor, Dr. Parvez Alam (and his wonderful family) for his patience and tireless supports for me, for every strong encouragement, for every new experience he gave me, for every cheer and laughter, and for every supports every time we met in Finland and Indonesia. Without his motivations and tough love for his students to reach perfection, all these studies will never be finished. I also want to thank Prof. Martti Toivakka, for every input, patience, and kind supports. For me, who also a high school teacher, his way of teaching has been very inspirational, calming, but able to bring the best of myself to learn and move forward. His motivational supports when I was on the verge of giving up always re-ignites my passion to go forward.

To Prof. Adolfo Rivero-Müller, I want to thank you for every random life stories you shared with me in his lab, for your patience and support when I did the DNA barcoding in his lab. Next, I want to thank Dr. Mari Nurmi, who has been so caring for our well-being, for being helpful during my experimental courses, and for giving me a lovely beanie.

On a personal level, I want to express my gratitude that I met the rest of PaF family, Mikka, Joel, Mukunda, Linda, Mengxiao, Vinay, Dimi, Rajesh, Ruut, Kofi, ÄV, Peter, Jani, and Diosa. In one note, I am sorry that I couldn't get more to know you all because I was there for just a short of time, I am also sorry for being so timid and did not manage to join you to most of the events you invited me. But without you all, I will not have a best story to tell during my time in Finland. Specifically, to Diosa and Jens (and Hime), thank you for the time you spend with me to explore the food of Turku and for the story you gave me. From Indonesia, I want to thank my best friends, Aji and Dwiki for their tireless support for me when I was struggling and so homesick.

I want to thank my family, my dad, Bunda Sofi, my mom, Uncle Odot, Aunt Win, and all my siblings and stepsiblings, especially my younger brother Arif, who has been relentlessly supporting me and cheering me up. To my late grandma, Siti Sarie who passed away in the last month of my stay in Finland (August 2016), I am sorry that I was not there to be with you on your last day, but I am happy to carry your wish to study to Europe. To my late grandpa,

Roeslan Soeroso, thank you for opening the gate of science for me. I hope you and grandma always be proud of me as now I have learned so far in science.

Close to the last but not least, I want to thank the love of my life, Ghea, who has been so patient with me. You have stayed with me during our long-distance relationship that separated us for 10,000 Km and 5-6 hours apart, and yet you are still here. Thank you for your smile, your kindness, your laughter, and everything you shared with me. I am sorry that in some time, I was so occupied with my works, and I was insensitive to you. But I want you to know, that whatever I did, next to as the form of my good deed I presented to God, I did my works to open the gate, so we can go together whenever we want in the future.

And at the last, I want to thank my fellow teachers of BTA Group, and ultimately to all my students that I have taught since January 2017. Thank you for being there. Thank you for listening to my story, including this part of my PhD degree and my moments when I was in Finland. Thank you for giving me a purpose as a teacher, as someone I entrusted with my knowledge. Sorry for too many improvements in teaching you, but you know? I do my best to make you understand from what I know, from the best professors and supervisors I learned with, so you will graduate as the best and you can be there at the best university you can go. I want you all to be successful in the future and when we meet again, please greet me with your smiles and tell me your story.

Bandung, November 2021

Adhityo Wicaksono

List of Publications

List of Included Publications

I. *The significance of pelvic fin flexibility for tree climbing fish*, A. Wicaksono, S. Hidayat, Y. Damayanti, D. S. M. Jin, E. Sintya, B. Retnoaji, and P. Alam, Zoology, **119**, 511–517 (2016).

II. *A mechanical piston action may assist pelvic-pectoral fin antagonism in tree-climbing fish*, A Wicaksono, S. Hidayat, B. Retnoaji, A. Rivero-Müller, and P. Alam, Journal of the Marine Biological Association of the United Kingdom, **98**, 1–11 (2017).

III. *The water-hopping kinematics of the tree-climbing fish, Periophthalmus variabilis*, A. Wicaksono, S. Hidayat, B. Retnoaji, and P. Alam, Zoology, **139**, 125750 (2020).

List of Supporting Publications

Articles currently being submitted

S1. *The morphologies of mudskipper pelvic fins in relation to terrestrial and climbing behaviour*, S. Hidayat, A. Wicaksono, A. Raharjeng, D. S. M. Jin, P. Alam, and B. Retnoaji, Proceedings of Zoological Society (2022; in press).

Author's Contribution

Publication I The author (AW), alongside SH, ES, and PA and supported by BR, performed the experimental work and data analysis of the experimental results from the laboratory and field observations. DSMJ performed the finite element analysis. YD examined the molecular dynamics model. AW, supervised by PA, wrote the article.

Publication II The author (AW), alongside SH and PA sampled the specimens in the field with the support of BR. AW was responsible for planning the experimental work, conducting the experiments, and analysing the experimental data. Together with ARM, AW performed DNA barcoding of the samples. AW, supervised by PA, wrote the article.

Publication III The author (AW), alongside SH, performed *in situ* field observation, recording the specimens for later analyses, with the support of BR and under the supervision of PA. Recordings were taken by Dwiki Mahendra Putra (independent videographer), and data sampling was done with the help of Immanuel Sanka (Talinn University of Technology) and Puspa Restu (Universitas Gadjah Mada). AW, supervised by PA, wrote the article.

Abstract

Mudskippers constitute a group of amphibious fish that have adapted for terrestrial locomotion. Some species in this group possess a tree-climbing ability. This study looks at the biomechanics behind this unique locomotion to assess their prospects for engineering applications. Our main objective in this study was to characterise the mudskippers' body features that relate to the terrestrial behaviour. We achieved this by developing simulation-based models to replicate the locomotive functions for engineering purposes.

We sampled the mudskippers through on-site (*in situ*) recording—employing cameras to capture both moving and still images—in order to conduct mechanical and kinematical analyses. We also collected off-site (*ex situ*) data, recording pelvic fin features to examine individual fin flexibility through finite element modelling (FEM). Additionally, we dissected fish to acquire data for an FEM focused on the skeletal system and musculature of the pectoral and pelvic fins. Furthermore, we obtained and analysed mucus samples from the mudskippers using Fourier transformation infrared (FTIR) spectroscopy. Following FTIR, we modelled the mucus chemical component through molecular dynamics simulations to assess its biomolecular interactions with the substrates on which the fish are commonly found. We conducted these simulations to test the hypothesis that the mucus provides the mudskipper with additional adherence support during vertical substrate attachment (i.e., tree-climbing).

The results of the molecular dynamics simulations show that the mucus chemical compound (hyaluronic acid [HA]) attracts the substrate compounds (calcium carbonate of the limestone, silica, and plant cell wall components: cellulose, hemicellulose, and lignin), indicating that the mucus positively supports mudskippers' adhesion. Complementing the mucus, the high-structural-flexibility pelvic fins enable the fish to grip the surface of the substrate. The mudskippers are unique in that their scales are covered by skin and mucus—most fish have skin covered by scales. Furthermore, their pelvic fins can be dispatched downward, like a piston passively using the inward push of pectoral fins as an efficient energy-saving method. Finally, the mudskipper can hop over water surfaces. It is able to conserve its kinetic energy throughout the water-hopping sequence to perform a long, efficient hop as an escape mechanism.

Learning from the results of this study, the biomechanics of the mudskipper can be modelled into various applications, some of which are detailed in this study. First, we consider the development of a controlled adhesion surface by applying the Stefan adhesion used by the mudskippers during climbing. The adhesion could be activated through mucus production at the interface area and deactivated using water, as the adhesion is governed by fluid viscosity.

Second, we consider the creation of a mudskipper-inspired robot/drone capable of walking on land and sticking to inclined surfaces. Third, we consider the development of elastic materials inspired by the skin-covered scales, though this would require further examination of mudskippers.

Abstrakt/Sammanfattning

Slamkrypare är en grupp amfibiska fiskar som kan röra sig på fast mark. Vissa av dem kan också klättra i träd. Biomekaniken som ligger bakom slamkryparnas unika rörelseförmåga studerades i hopp om att hitta möjligheter för tekniska applikationer. Huvudsyftet med studien var att karakterisera några av slamkryparens kroppsfunktioner som är relaterade till dess unika beteende. Karakteriseringen gjordes genom utveckling av simuleringsbaserade modeller för att kunna återskapa funktionerna för tekniska ändamål.

Slamkryparna studerades genom videoinspelning och fotografering på provtagningsområdet (*in situ)*. Samtidigt samlades ytterligare uppgifter in utanför provområdet *(ex situ)* för registrering av bäckenfenornas egenskaper för finit elementmodellering (FEM), där fenornas flexibilitet undersöktes. Dissekering av fiskar utfördes också där ytterligare data insamlades för en annan FEM-modellering som fokuserade på skelettsystemet samt på bröst- och bäckenfenornas muskulatur. De inspelade videofilmerna användes för mekanisk och kinematisk analys. Dessutom togs prover av slamkryparnas slem, vilka analyserades med hjälp av Fourier transform infraröd spektroskopi (FTIR). Efter FTIR-spektroskopin modellerades slemmets kemiska sammansättning med hjälp av molekylär dynamik-simuleringar där slemmets biomolekylära interaktioner med de substrat som fisken allmänt förekommer på studerades. Dessa simuleringar gjordes för att bekräfta interaktionerna mellan slem och substrat, eftersom en hypotes var att slem ger ytterligare stöd när slamkryparen håller sig fast vid ett vertikalt substrat, t.ex. när den klättrar i träd.

Molekylär dynamik–simuleringarna visar att den kemiska sammansättningen hos slemmet (hyaluronsyra eller HA) attraherar föreningar hos substratet (kalciumkarbonat av kalksten och kiseldioxid, samt komponenterna cellulosa, hemicellulosa och lignin hos växtcellernas väggar), vilket indikerar att slemmet bidrar till fiskens adhesionsförmåga. Som komplement till slemmet tillåter bäckenfenornas höga strukturella flexibilitet fisken att greppa substratets yta. Dessutom är slamkryparnas fenor och kropp täckta av fjäll, vilka täcks av skinn, som i sin tur är täckt av slem. Detta till skillnad från andra fiskar, vars skinn täcks av fjäll. Slamkryparen kan också sträcka sina bäckenfenor nedåt, varvid de fungerar som en kolv som passivt använder bröstfenornas inåtriktade tryck mot kroppen, vilket ger en effektiv och energibesparande rörelsemetod. Slutligen kan slamkryparen hoppa över en vattenyta, och kan spara sin användning av kinetisk energi över hoppsekvensen och utföra en lång, effektiv serie hopp som en flyktmekanism.

Resultaten från denna studie kan hjälpa modellering av slamkryparens biomekanik i olika tillämpningar. Vissa hypotetiska designkoncept ingår i

denna studie. Dessa inkluderar en kontrollerad adhesionsyta som fungerar via samma Stefan-adhesion som används av fisken när den klättrar, dvs. adhesionen kan aktiveras av slemproduktion i gränssnittsområdet och avaktiveras genom att slemkoncentrationen minskas med vatten. Detta eftersom vidhäftningen styrs av vätskans viskositet. En slamkryparinspirerad robot/drönardesign som kan gå på land och fästa sig vid lutande ytor föreslås. Ett annat koncept är att skapa elastiska material inspirerade av slamkryparens hudtäckta fjäll, men detta kräver ytterligare, framtida undersökningar av slamkryparen.

Abbreviations and Nomenclatures

BCF	Body-caudal fins swimming type
CAD	Computer-assisted design
CFM	Computational fluid modelling
DH	Denavit-Hartenberg parameters
DOF	Degrees of freedom
EE	End of effector
FEA	Finite element analysis
FEM	Finite element modelling
FTIR	Fourier-transform infrared spectroscopy
HTM	Homogenous transformation matrix
MPF	Median paired-fins swimming type
MRF	Magnetorheological fluid

Table of Contents

1. Introduction

The mudskipper is a unique fish capable of employing a terrestrial mode of locomotion. Out of water, it uses specialised pectoral fins as crutches to move and its pelvic fins to stabilise its body as it moves forward. Unlike most fishes, which live almost entirely in the water, mudskippers are generally amphibious. In fact, studies by Tamura et al. (1976) and Low et al. (1988) show that one mudskipper species—the giant mudskipper, *Periophthalmodon schlosseri* (Pallas 1770)—is better adapted to the terrestrial environment than the aquatic environment. This is also evident in another genus observed in this study, *Periophthalmus*, which spends most of its time on a solid substrate of muddy soil rather than in the water.

Crutching is the mudskipper's main mode of terrestrial locomotion (Harris 1960, Sayer 2005). They walk by using their pectoral fins as two crutches while using their pelvic fins to balance their movement. Mudskippers have also been observed performing other unique modes of locomotion. During our study, we learned that at least one mudskipper genus, *Periophthalmus*, is able to climb and stick to inclined and even vertical substrates (e.g., tree roots, glass aquaria). Furthermore, it can hop onto water surfaces to escape incoming threats from land; when we approached the mudskipper, it moved to another part of the muddy shore by hopping instead of swimming. Leaning into these field observations, the biomechanical characterisation of the mudskipper—especially the dusky-gilled mudskipper, *Periophthalmus variabilis* (Eggert 1935), which has unfused pelvic fins—constitutes the main objective of this study. Additionally, for comparison, we observed the slender mudskipper, *Periophthalmus gracilis* (Eggert 1935), a smaller mudskipper with similar pelvic fins and body morphology, and Boddart's goggle-eyed goby mudskipper, *Boleophthalmus boddarti* (Pallas 1770), which has fused pelvic fins. We also observed an ornate goby, *Istigobius ornatus* (Rüppell 1830) for a non-mudskipper fish comparison.

The mechanism that mudskippers use to adhere to inclined and vertical substrates has yet to be clearly detailed. Similarly, the biomechanics of how the skeletal structure and musculature synergistically assist the pectoral and pelvic fins during terrestrial locomotion requires greater attention. Additionally, the biomechanics of how the mudskipper—in this case, *P. variabilis*—hops on water is still unknown. Hence, further biomechanical analysis of mudskippers will provide a greater understanding of how the amphibious fishes move on both land and water.

The aim of this study is to understand the biomechanics behind mudskippers' unique modes of locomotion. Inspired by the newly described biomechanical characteristics, the mudskippers can be modelled to create new engineering designs or improve existing ones through our template of bioinspiration for biomimetics and bionic engineering. Therefore, this study has two main

objectives: 1) biomechanical characterisation of mudskippers' attachment to substrates, skeletal-muscular synchronisation during terrestrial locomotion, and body kinematics during water-hopping and hopping-related movements; and 2) adaptation of mudskippers' biomechanics into the bioinspired design of vertical substrate attachment.

The pelvic fins of *P. variabilis*, which has unfused pelvic fins, and *B. boddarti*, which has fused pelvic fins, are compared, modelled, and characterised in **Paper I**. **Paper II** details the differences in how the mudskippers (*P. variabilis* and *P. gracilis*) and the non-mudskipper fish (*I. ornatus*) deal with the terrestrial mode of locomotion. Finally, **Paper III** elaborates the kinematics and mechanics of the water-hopping and hopping-related movements of *P. variabilis* based on video analysis. The bioinspiration of the mudskippers' substrate attachment and the simplified modelling of a mudskipper-inspired robot—which were not included in any previously published papers—were the next objectives of this study.

Kutschera and Eliott (2013) assert that the mudskipper is a good model for modern terrestrial adaptation and behaviour among fish. Through deeper research into the mudskipper, future researchers could achieve a breakthrough in amphibious biorobotic design. This amphibious robot could later be used to advance engineering designs and products and to achieve a greater understanding of how the mudskipper and other terrestrial fish adapt to the terrestrial environment as a form of "learning by making."

2. Background Reviews

2.1 General Fish Locomotion Biomechanics: Aquatic, Terrestrial, and Aerial

2.1.1 In General

Biomechanics refers to the study of the mechanics of living beings. It often entails the observation of kinematics and kinetics. Kinematics explains objects' positional changes, velocity, and acceleration. Such observation may involve the description of movements, displacements, or transformations without reference to the causes of motion (i.e., regardless of the force). For example, while swimming, a fish could either undulate or oscillate its core body length (from the cranial tip to the caudal tip). On the other side, kinetics elaborates the causes of objects' motion. Such observation may involve the measurement of positional changes, velocity, acceleration, and energy, among others. For example, caudal fins could oscillate laterally (sideways) at a specific velocity to compensate for fluid viscosity and propel the body forward.

Throughout the course of evolution, fish have adapted to various modes of locomotion. This section briefly details the aquatic (in the water; e.g., swimming), terrestrial (on land; e.g., crutching), and aerial (airborne; e.g., hopping, gliding) modes of locomotion.

2.1.2 Aquatic

Fish are aquatic organisms that—aside from specially adapted species—spend the entirety of their life in the water. There are two main swimming types among fish: the body-caudal fins (BCF) type and the median paired-fins (MPF) type. BCF swimmers (Fig. 1A) rely on the proportion of core body movements and flexibility to either undulate or oscillate to move forward. This type can be further subdivided by the body's proportions (Sfakiotakis et al. 1999):

1. **Anguiliform**: most of the body length undulates laterally (e.g., eel)
2. **Subcarangiform**: the caudal half of the body undulates laterally (e.g., trout)
3. **Carangiform**: less than the caudal half of the body undulates, but as beam length decreases, it leans toward lateral oscillation (e.g., jack mackerel)
4. **Thunniform**: only the caudal part of the body and the caudal fins move laterally (e.g., tuna)
5. **Ostraciiform**: only the caudal fins oscillate laterally (e.g., boxfish)

MPF swimmers (Fig. 2.1B), on the other hand, rely on the movements of paired fins of their body to move forward. This includes either a single set of paired fins (e.g., pectoral fins only) or combined fins (e.g., dorsal-anal fins). This type, based on Sfakiotakis et al. (1999), can be subdivided further as:

1. **Rajiform**: the large pectoral fins undulate dorsoventrally (e.g., manta ray)
2. **Diodontiform**: the large pectoral fins undulate laterally (e.g., porcupinefish)
3. **Labriform**: the pectoral fins oscillate (e.g., wrass)
4. **Amiiform**: the long dorsal fin undulates laterally (e.g., bowfin)
5. **Gymnotiform**: the long anal fin undulates laterally (e.g., knifefish)
6. **Balistiform**: the dorsal-anal fins undulate laterally (e.g., triggerfish)
7. **Tetraodontiform**: the dorsal-anal fins oscillate laterally, either in phase or interchanged between one and another (e.g., pufferfish)

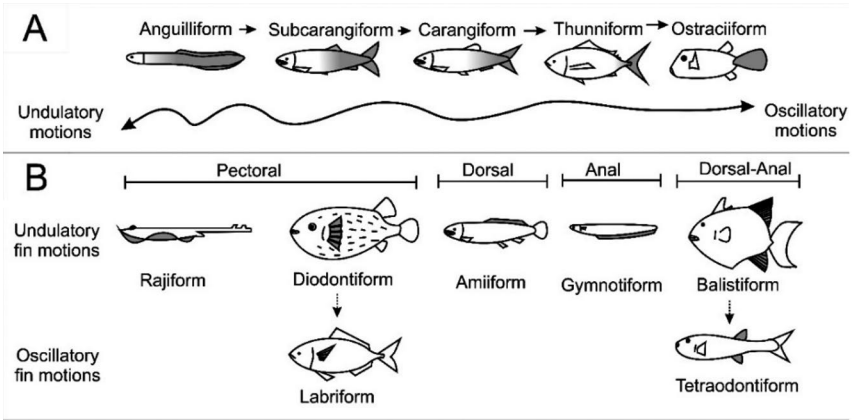

Figure 2.1. General fish swimming types, split between body or caudal fin movements (BCF; A) and median or paired fin movement (or MPF; B). Shading depicts the body section that contributes to fish propulsion (inspired by Pough et al. 2005 and Sfakiotakis et al. 1999).

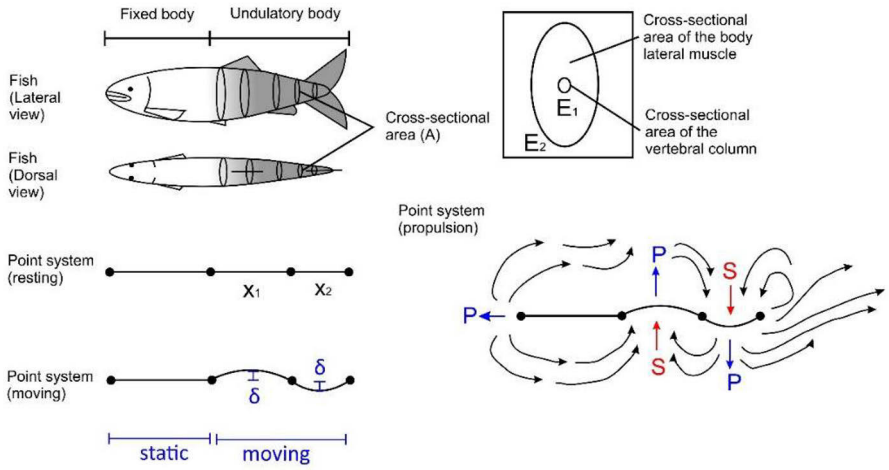

Figure 2.2. Schematics of fish swimming (subcarangiform type) reliant on the undulatory part of the body as the cross-sectional area (A) of different segments. Resting and moving states are described through a system of four points with x as the length per segment. The deflection expressed by the undulation in δ generates push and pull in the water flow, resulting in pressure force (P) and suction force (S), respectively. The combining forces of pressure and suction in water generate vortices around the fish body (subfigure inspired by Sfakiotakis et al. 1999); the flow then goes backward, pushing the fish forward. The fish cross-section has its own elastic moduli: E_1 for the bone and E_2 for the lateral musculature.

Swimming type dictates how fish generate controlled suction and pressure to produce a stream of vortices behind their body (Fig. 2.2). By assuming that the caudal body forms an S-shape while swimming, we can divide the moving body of BCF-type swimmers into a four-point system (Fig. 2.2), with each line connecting two points having its own length (x). When the caudal body and caudal fins undulate, the beam deflection (δ) pushes the body away from its axis, and the pull in the water generates suction forces. As undulating fish have a certain degree of flexibility, as with springs with a certain spring constant (k), we may calculate the generated force from the stroke as (F) in Eq. 2.1.

$$F = kx \qquad (2.1)$$

The cross-sectional surface areas (A) may vary along the length of the fish body. From this, the Euler-Bernoulli formula (Eq. 2.2) shows the correlation between beam deflection and the applied load during active movements. Here, the beam of body curvature (w) describes the beam deflection (modelled as a one-dimensional object), with x as the beam length, E as Young's elastic

modulus, I as the second moment area of the beam cross-section, and q as the distributed load.

$$\frac{d^2}{dx^2}\left(EI\frac{d^2w}{dx^2}\right) = q \qquad (2.2)$$

The second moment of inertia of the beam (I) in a round-shaped body can be measured through Eq. 2.3, and this can be approximated into Eq. 2.4 with r and d as the radius and diameter, respectively. This measurement assumes that the beam has a circular cross-section (A).

$$I = \int y^2 dA \qquad (2.3)$$

$$I = \frac{\pi}{4}r^4 = \frac{\pi}{64}d^4 \qquad (2.4)$$

The main purpose of the body bending during swimming is to overcome water viscosity and provide thrust to the net force. Upon moving forward, the fish body's undulation/oscillation movements must overcome the vortex suction, leading to the generation of streets of vortices known as Karman street or reverse Karman street vortices (Triantafyllou and Triantafyllou 1993). The ratio between undulation and oscillation that leads to the vortex shedding of a fish body (f) with a certain length (L) and flow velocity (U) is here described as a dimensionless number—the Strouhal number (S_r) (Eq. 2.5). If the fluid velocity overcomes the undulation/oscillation, Karman street vortices are generated, meaning the fish cannot move forward. If the undulation/oscillation wins, reverse Karman street vortices are generated, meaning the fish can move forward (Triantafyllou et al. 1991; Triantafyllou et al. 1993; Triantafyllou and Triantafyllou 1993; Read et al. 2003).

$$S_r = \frac{fL}{U} \qquad (2.5)$$

In addition to the active feature of the fish, as described above, the surface feature of the fish is equally important (i.e., whether the fish body morphology is streamlined enough in the water). There is another dimensionless number that describes whether fluid flow is laminar (streamlined) or turbulent—the Reynolds number (Re), measured with ρ as fluid density, U as flow velocity, L as specified beam length, μ as dynamic viscosity, and v as kinematic viscosity (Eq. 2.6). If the number is low, the flow is laminar; if the number is high, the flow is turbulent. If the fish body is more streamlined, the fish can move easily with less body movement required for propulsion, as the water flows easily around it; this feature is common among high-speed swimming fishes (e.g., swordfish). If the fish body is less streamlined, the water around the fish flows turbulently, reducing its swimming efficiency.

$$Re = \frac{\rho UL}{\mu} = \frac{UL}{v} \qquad (2.6)$$

2.1.3 Terrestrial

Lobe-finned fishes that lived during the Silurian period (e.g., *Eusthenopteron*) have previously been assumed to have evolved certain fin features to enable their transition to land (Pough et al. 2005). This hypothesis, however, has since been abandoned as paleoanatomical evidences indicate that the bone structures of *Eusthenopteron* are more suitable in deep aquatic waters, rather than in shallow waters or in terrestrial environments (Laurin et al. 2007). In comparison, present-day lobe-finned fishes are not adapted for this terrestrial adaptation and adapted more for aquatic locomotion, such as coelacanths (Mauritius coelacanth, *Latimeria chalumnae* [Smith 1939] and Indonesian; Manadonese coelacanth, *L. menadoensis* [Pouyaud et al. 1989]) and lungfish (African lungfish, *Protopterus* sp.; Australian lungfish, *Neoceratodus* sp.; South American lungfish, *Lepidosiren* sp.). The lobed fins of the coelacanth, despite their similarities to the ancient lobe-finned fish that brought the dawn of the tetrapods, are used exclusively for swimming—not walking on land or the seafloor (Fricke and Hissmann 1992). As with lungfish, they use their fins only for aquatic locomotion, employing their body muscles instead for terrestrial locomotion (Horner and Jayne 2014; Falkingham and Horner 2016).

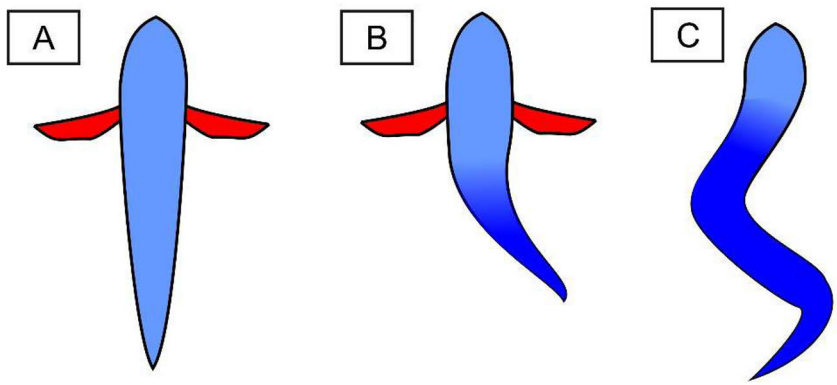

Figure 2.3. Three modes of terrestrial locomotion in fish (inspired by Pace and Gibb 2014): Appendage-based (A), axial-appendage-based (B), and axial-based (C). Red indicates the moving appendages, light blue is the body axis, and the darker blue indicates the moving body axis sections.

In general, there are three types of locomotion observed in modern terrestrial fishes: appendage-based, axial-based and axial-appendage-based (Pace and Gibb 2014; Fig. 2.3). Appendage-based locomotion (Fig. 2.3A) is assisted by movements driven by the appendages (e.g., fins). The walking cavefish (*Cryptotora thamicola* [Kottelat 1988]) using appendage-based locomotion using

the active movements of its paired fins (i.e., pectoral and pelvic fins) active movements, in a similar way to a salamander that uses its legs in diagonal-couplet lateral sequence gait (Flammang et al. 2016). Mudskippers use their pectoral fins for a movement known as crutching. This movement entails extension of pectoral fins while the pelvic fins open up to stabilise the stabilise the body of the fish (Harris 1960; Gibson 1986; Sayer 2005). Axial-based locomotion (Fig. 2.3C) is assisted by body axis bending (i.e., into C or J-shape) and straightening (recovery) to propel the fish forward. An example of axial-based terrestrial locomotion is the Pacific leaping blenny (*Alticus arnoldorum* [Curtiss, 1938]), which relies on its body axis caudal section equipped with wide caudal fins to bend and push the substrate caudally, moving the fish forward (Hsieh 2010). Axial-appendage-based locomotion (Fig. 2.3B) combines the traits of both axial and appendage-based locomotion. An example is the *Polypterus senegalus* (Lacepède 1803), which uses the combination of pectoral fins and its body axis to move (Standen et al. 2016). A unique example is the climbing perch (*Anabas testudineus* [Bloch 1792]), which uses the combination of its specially-adapted gill subopercular parts and its body axis to move forward (Davenport and Matin 1990).

When a terrestrial fish tethers on its own fins—or, similarly, a tetrapod on its own limbs—the pressure (P) on the fins or limbs depends on the given force, in this case the force (F) of body weight (W, measured by mass, m, times gravitational force, g) per substrate contact surface area (A) of the tip of fins or limbs, as shown in Eq. 2.7 below.

$$P = \frac{F}{A} = \frac{W}{A} = \frac{mg}{A} \qquad (2.7)$$

Equation 2.7 shows that, as the surface area of the tip of fins or limbs increases, the pressure exposed to the fins or limbs decreases, reducing the potential damage to the fins (pectoral and pelvic) or limbs (front and hind), as it supports the body weight. Thus, it is important to have 1) enlarged ray areas of fins with adequate radial contact areas to provide shock reduction for terrestrial fishes or 2) expandable surface areas of limbs through retractable finger digits with joints to provide shock absorbance for amphibious tetrapods. Varying pressure reduction through contact area size can be seen in Fig. 2.4.

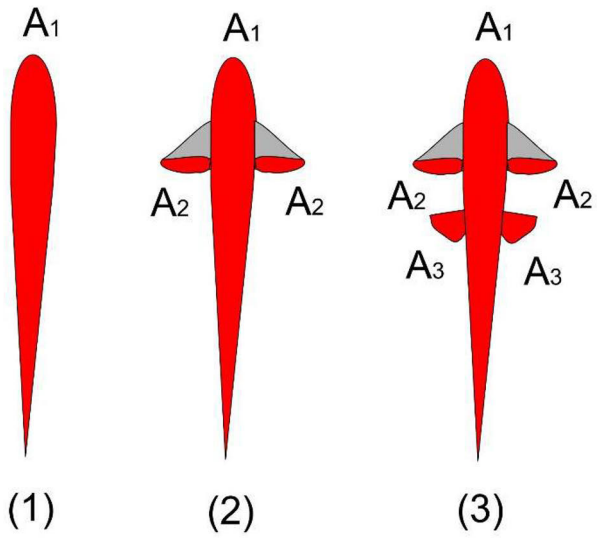

Figure 2.4. Terrestrial fish surface of the ventral area that contacts (A) the substrate with only the body (1), body with pectoral fins (2), and body with pectoral and pelvic fins (3).

Despite force by body weight (w, or mass, m, multiplied by gravity acceleration, g) being assumed to be equal for all three fishes in Fig. 2.4, the pressure applied across all three conditions is reduced through additional lower-body substrate-contact surface area. Fish with all pectoral and pelvic fins extended have the lowest pressure through contact with the solid substrate. From this analysis, we can assume that the mudskipper, which uses both pectoral and pelvic fins for terrestrial locomotion, may have an advantage in their adaptation to walk on hard terrestrial substrate relative to fish that rely on their body ventral surface or pectoral fins. Additionally, large body surface area is favourable to facilitate friction, allowing better grip control to the substrate. Although the fish body and fins are lubricated by mucous secretion, some area (e.g. parts of pectoral and pelvic fins, and caudal area) that assist active locomotion could provide enough friction to facilitate movements.

2.1.4 Aerial

Certain fish exhibit aerial modes of locomotion, normally as a method for escaping from predators. If aerial movement is achieved briefly, it can be referred to as hopping. However, among specially adapted fish like flying fish (family: Exocoetidae), the aerial period extends beyond hopping, as the body relies on large, unique pectoral fins as wings to glide for long distances and pelvic

fins (among four-winged flying fishes) as elevators analogous to planes (Davenport, 1994).

Both gliding and hopping are always initiated by caudal fin movements to taxi and take off (Fig. 2.5). For gliding, the flying fish undulates its caudal region and heterocercal caudal fins (unequal in size between the upper and lower lobes; in this case, the lower lobe is larger) in cyclic, rapid, lateral movements to taxi before going airborne (Davenport, 1994). Similarly, water-hopping, which is detailed in this study (**Paper III**), involves shorter take-off sequences before going airborne.

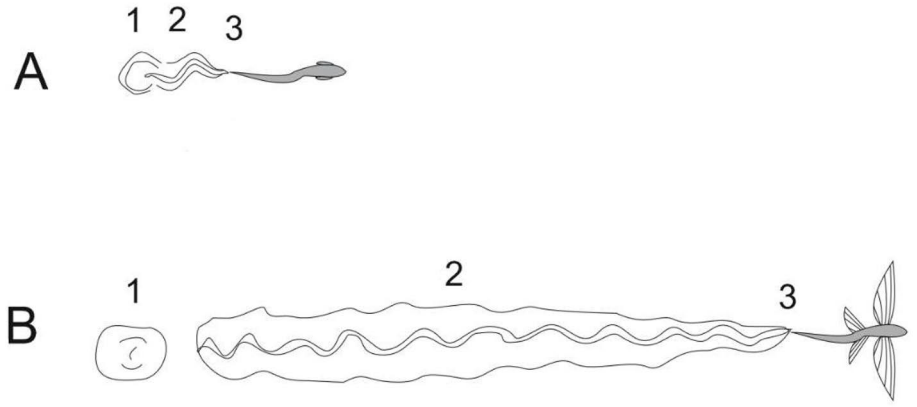

Figure 2.5. The hopping mudskipper (A) and gliding flying fish (B) move from their initial position (1), taxi using their caudal fins' cyclic lateral movements (2), and take off (3). Figure featured in Wicaksono et al. (2020) (**Paper III**).

The take-off process aims to generate kinetic energy as the fish speeds forward. Kinetic energy (K_e) is a function of mass (m) and velocity (v) (Eq. 2.8), meaning this energy is lost (i.e., kinetic energy loss, K_{e_LOSS}) during the air-to-water transition, as it moves forward until it stops (Eq. 2.9).

$$K_e = \frac{1}{2}mv^2 \qquad (2.8)$$

$$K_{e\_LOSS} = \frac{K_{e\_AIR}(d)}{K_{e\_WATER}(d)} \qquad (2.9)$$

Following the same concept, migratory fish like salmon can hop against the height gradient by initially accelerating using an S-start (i.e., body in an S-shape to spring forward) and then swimming with a speed burst to the moment at which it propels itself in the form of an arch (Fig. 2.6) (Lauritzen et al. 2005; 2010). This speed build-up is also used by the salmon to generate enough kinetic

energy to propel itself through vertical water columns as it moves from lower ground to higher ground to reach its spawning area.

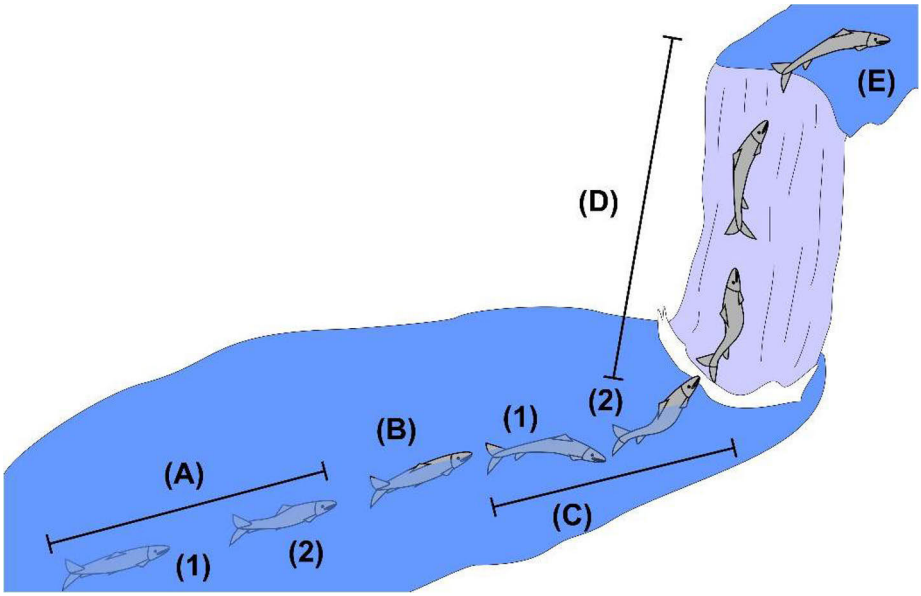

Figure 2.6. The sequence of the salmon hopping over the waterfall (according to Lauritzen et al. 2010). The salmon start by swimming slowly to the base of the boil of the waterfall (A1–A2) and rotating their bodies to face the water surface (B). The salmon then make S-starts, arching their bodies (C1), rapidly beating their tails, and accelerating through the boil to take off (C2). After taking off, the salmon travel through the air (D) toward the crest of the waterfall while continuing to beat their caudal fins (E).

2.2. Mudskipper

"Mudskipper" refers to the group of fishes in the Oxudercidae family. Mudskippers were previously categorised as Gobiidae (Murdy 1989) until recent molecular studies suggested that oxudercine gobies are paraphyletic to amblyopine gobies (family Gobiidae; subfamily Amblyopinae) (Agorreta et al. 2013). Hence, the mudskipper was moved to the Oxudercinae subfamily under the Oxudercidae family. There are 10 genera of mudskippers, and all of them are known for their aquatic-terrestrial transitional habitat (Murdy 1989):

1. *Apocryptes*
2. *Apocryptodon*
3. *Boleophthalmus*
4. *Oxuderces*

5. *Parapocryptes*
6. *Periophthalmodon*
7. *Periophthalmus*
8. *Pseudoapocryptes*
9. *Scartelaos*
10. *Zappa*

Of these ten genera, only four exhibit air-breathing capabilities (*Periophthalmus, Periophthalmodon, Boleophthalmus, Scartelaos*). Three are facultative air-breathers (only on hypoxia or increased metabolic demand; *Apocryptes, Pseudoapocryptes, Zappa*), and the remaining three have not been documented to possess air-breathing capabilities (*Parapocryptes, Oxuderces, Apocryptodon*) but are able to gulp air (Graham and Lee 2004).

Some of the species have been known by previous studies to possess cutaneous respiration in addition to gill respiration to aid in their terrestrial behaviours. This adaptation includes the vascularisation of skin with many subcutaneous capillaries to allow for gas exchange (Park 2002). It also includes a large gill operculum, which is able to retain more water over a longer period of time after leaving the water (Piper 2007).

Aside from physioanatomical features, mudskippers are equipped with a pair of modified pectoral fins (Kutschera and Eliot 2013), pelvic fins (Sayer 2005), and caudal fins (Pace and Gibb 2009) to support terrestrial locomotion. Their pectoral fins act as crutches that propel the fish forward (Gibson 1986). The weight supported during terrestrial locomotion by the mudskipper pectoral fins is comparable to that of tetrapods' (e.g., salamander) front and hind limbs (Kawano and Blob 2013). The pelvic fins function as pads that stabilise the body when the pectoral fins stroke backwards (Sayer 2005). Interestingly, mudskippers' pelvic fins vary in type (Polgar 2010) (Fig. 2.7).

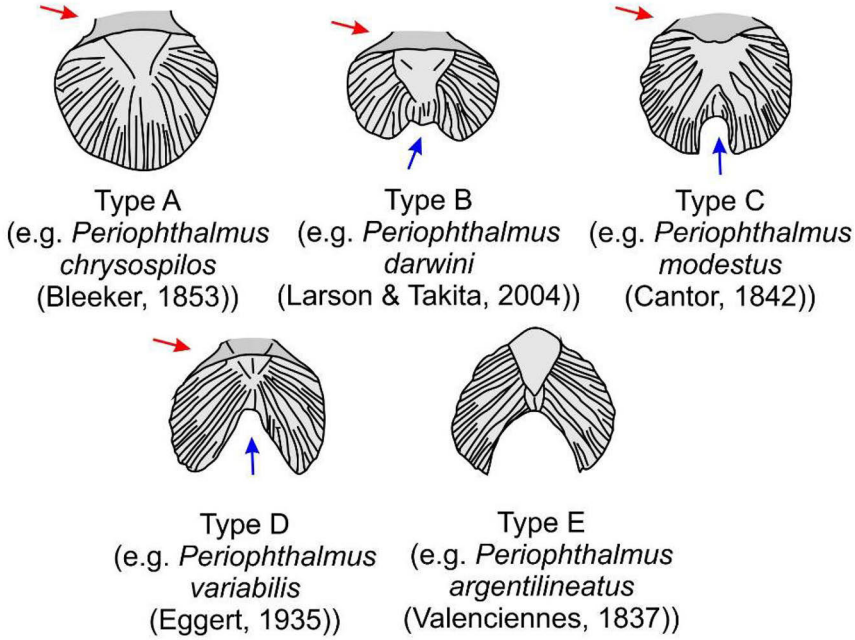

Figure 2.7. Various types of pelvic fins, as shown in different *Periophthalmus* species. Types A–D have the pelvic fins united anteriorly to the pelvic frenum (red arrows). Type A comprises fused fins. Types B–D are semi-unfused fins connected posteriorly by basal membrane (blue arrows). Type E comprises totally unfused fins with no frenum unification or basal membrane connections. Redrawn from Polgar (2010).

Some mudskippers, as seen in this study, are able to climb substrates with higher elevations (e.g., bamboo poles, tree logs), earning them the title of "the tree-climbing fish". Some small mudskippers, such as *Periophthalmus*, are able to stick to vertical glass aquaria. This capability is thought to be supported by the extension of unfused pelvic fins paired with skin-secreted mucous—achieving Stefan adhesion (i.e., adhesion between two parallel plates connected by a viscous fluid; Stefan, 1874 *cit*. Ewoldt et al. 2011) instead of using suction force (e.g., pelvic suctorial organ in lumpsucker fish [Cyclopteridae and Liparidae] [Budney and Hall 2010], modified dorsal fins in remora fish [Britz and Johnson 2012]).

The fluid-mediated adhesion (F_{WA}), or wet adhesion force, is the force that commonly occurs between a body and a substrate surface with the help of fluid (Dirks 2014). The force originally comes from fluid-to-environmental interactions of capillary and adhesion force. For the following equations, adhesion can be modelled using the separation distance (h), the adhered object radius (R), and the contact angle of the mediating fluid (θ).

First, there is force (F_{ST}) caused by the fluid's surface tension (γ), as shown in Eq. (2.10).

$$F_{ST} = 2\pi\gamma R \qquad (2.10)$$

The force from the pressure difference between the outside and inside of the curved surface (the fluid meniscus surface), which forms the boundary between gas and liquid regions, is called Laplace pressure (F_{Lap}) (Eq. 2.11).

$$F_{Lap} = \pi\gamma\left(\frac{2\cos\theta}{h} - \frac{1}{R}\right)R^2 = \pi\gamma R^2\left(\frac{2R\cos\theta - h}{hR}\right) \quad (2.11)$$

Stefan adhesion force (F_{Stef}) is adhesion aided by viscous mucous fluid, measured with η as the fluid (i.e., mucous viscosity) and period of time (t) (Eq. 2.12).

$$F_{Stef} = \frac{3\pi\eta R^4}{2h^3}\frac{dh}{dt} \qquad (2.12)$$

The combined force of Laplace pressure (Eq. 2.11) and surface tension (Eq. 2.12) constitutes the capillary force from the fluid and the surface ($F_{capillary}$). Stefan adhesion force constitutes the force of adhesion from the viscous fluid ($F_{viscous}$). Combined, the wet adhesion force is defined by Eq. 2.13 (Dirks 2014).

$$F_{WA} = F_{capillary} + F_{viscous} = F_{ST} + F_{Lap} + F_{Stef} \qquad (2.13)$$

Some mudskippers (e.g., *Periophthalmus* and *Periophthalmodon*; personal observation) tend to remain in terrestrial environments even when threatened. When the fish is disturbed (e.g., poked), they tend to escape by rapidly hopping on the water surface rather than swimming, making them even more unique (**Paper III**).

2.3. *In silico* modelling method examples for biomechanics

2.3.1 Finite Element Modelling

In trying to measure two-dimensional planes or three-dimensional objects, they sometimes have structures or surfaces that are too complicated or abstract to measure. To deal with this, we can use a discretisation or partitioning method to transform the plane or object into a mesh comprising uniform structural units called elements (Johnston et al. 1991; Gibson et al. 2003; Alam 2004). The elements are connected to one another by nodes. As more elements are used to represent the whole object, the measurement becomes more similar to the actual condition (Fig. 2.8). Element shapes can become more representative through the inclusion of more nodes. Of course, more elements generally means longer

computation times. The elemental shapes are ordered by Lagrange interpolation polynomials; hence, they are called Lagrangian elements (Courant 1943). The order of polynomials aligns with their elemental node numbers; examples are shown with triangular and polyhedral elements in Table 2.1. The procedure for simulating a physical condition using these elements is called finite element modelling (FEM) or, for analysis, finite element analysis (FEA).

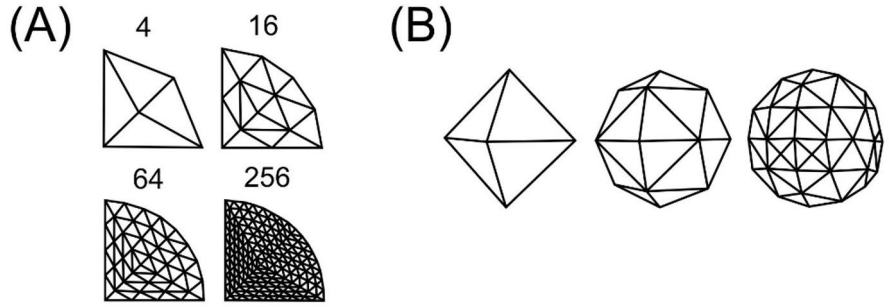

Figure 2.8. Four two-dimensional objects with different mesh densities (number of elements) to represent a quarter of a circle (A; redrawn from Falk and Tu [2000]) three two-dimensional representations of three-dimensional objects with different mesh densities to represent a sphere (B; redrawn from kronuz.io).

Table 2.1 The order of Lagrangian elements with polynomials and number of nodes (source: FEMwiki.wikidot.com; *cit*. Courant, 1943).

	Triangles		Tetrahedra	
Order	Polynomials	Nodes no.	Polynomials	Nodes no.
0	1	1	1	1
1	$1 + x + y$	1 + 2	$1 + x + y + z$	1 + 3
2	$1 + x + y + x^2 + xy + y^2$	1 + 2 + 3	$1 + x + y + x^2 + xy + xz + y^2 + yz + z^2$	1 + 3 + 5
k	…	$1 + 2 + \ldots + (k + 1)$	…	$1 + 3 + \ldots + ((k + 2)(k + 1)/2)$

Nodes in spatial geometry serve to connect points of elements. For example, they could be used to simulate a model of the effect on local pressure generated by the given external forces, as force (F) is the result of stiffness (k) and displacement (δ; Eqs. 2.14–2.15). Additionally, stiffness is the inverted function of flexibility (C), hence c = 1/k.

$$F = k\delta \qquad (2.14)$$

$$\delta = CF \qquad (2.15)$$

Thus, we can set Eqs. 2.14 and 2.15 to the nodal system as a function of the matrix constrained by the degree-of-freedom (DOF) number and the nodal numbers (Eq. 2.14 to Eqs. 2.16–2.17; Eq. 2.15 to Eqs. 2.18–2.19). The cumulative DOF number within the structure is marked by n; the maximum number of force-transmitting nodes inside the structure is x. The concept is also applicable to other forms of FEM measurement (e.g., material stress modelling, computational fluid modelling, heat conduction, acoustics).

$$\{F\} = [k]\{\delta\} \qquad (2.16)$$

$$\begin{Bmatrix} F_1 \\ \vdots \\ F_n \end{Bmatrix} = \begin{bmatrix} k_{11} & \cdots & k_{1n} \\ \vdots & \ddots & \vdots \\ k_{x1} & \cdots & k_{xn} \end{bmatrix} \begin{Bmatrix} \delta_1 \\ \vdots \\ \delta_n \end{Bmatrix} \qquad (2.17)$$

$$\{\delta\} = [C]\{F\} \qquad (2.18)$$

$$\begin{Bmatrix} \delta_1 \\ \vdots \\ \delta_n \end{Bmatrix} = \begin{bmatrix} C_{11} & \cdots & C_{1n} \\ \vdots & \ddots & \vdots \\ C_{x1} & \cdots & C_{xn} \end{bmatrix} \begin{Bmatrix} F_1 \\ \vdots \\ F_n \end{Bmatrix} \qquad (2.19)$$

One application often used in biomechanics, including in this study (**Paper I and Paper II**), is material stress modelling aimed at measuring material stiffness. Here, the von Mises stress envelope model provides greater flexibility than the previously used Tresca stress envelope model. According to Henry Tresca, a material would fail if stress exposure (σ_T) is bigger than the material's maximum stress (σ_{max}) (Eq. 2.20).

$$\sigma_T = \sigma_1 - \sigma_3 > \sigma_{max} \qquad (2.20)$$

The stress envelope modelled by von Mises is more flexible (Fig. 2.9), as it can be used to visualise stress distribution in two-dimensional and three-dimensional structures for both material elasticity and failure models. Thus, the von Mises stress envelope, due to its flexibility, can be applied to multiple biological structures, some of which are rather irregular. The von Mises stress yield (σ_v) can be measured as Eq. 2.21.

$$\sigma_v = \sqrt{(\sigma_1 - \sigma_3)^2 + (\sigma_3 - \sigma_2)^2 + (\sigma_2 - \sigma_1)^2} \qquad (2.21)$$

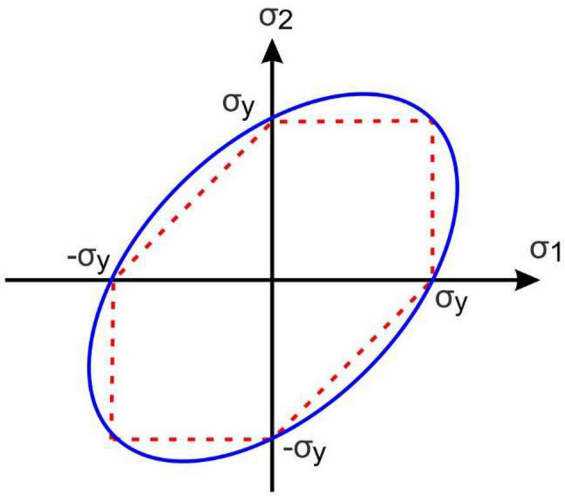

Figure 2.9. Two-dimensional projection of von Mises stress envelope (blue oval line) vs. Tresca stress envelope (red dashed line). The area covered by von Mises exceeds that of Tresca, making von Mises's criteria more flexible. Redrawn from Oujebbour (2014).

In testing material stiffness, the Young's modulus or elastic modulus (E) is obtainable by measuring the stress (σ) per strain (ε) (Eq. 2.22). The Poisson's ratio (ν; Eq. 2.23), which determines the compressibility of a solid material is obtainable by measuring the negative of the transverse strain ($\varepsilon_{transverse}$) per axial strain (ε_{axial}).

$$E = \frac{\sigma}{\varepsilon} \qquad (2.22)$$

With σ as stress, and ε as material strain.

$$\nu = -\frac{\varepsilon_{transverse}}{\varepsilon_{axial}} \qquad (2.23)$$

Ultimately, FEM is a powerful tool in engineering. The applications of FEM are vast so long as it is supported by a strong computer processor and program. FEM can be used to gain a greater understanding of the biomechanics of living organisms, especially since irregular biological morphologies can be simulated. Additionally, we can use FEM for biomimetic optimisation by modelling designs based on living organisms, simulating them, and revising them until we achieve optimal results.

2.3.2 Molecular Mechanics

On the molecular level, compounds from individual molecules can interact with one another. Between each individual molecules, there are attracting and repulsing forces. To understand these interactions, we can use computer-based modelling to simulate molecular dynamics.

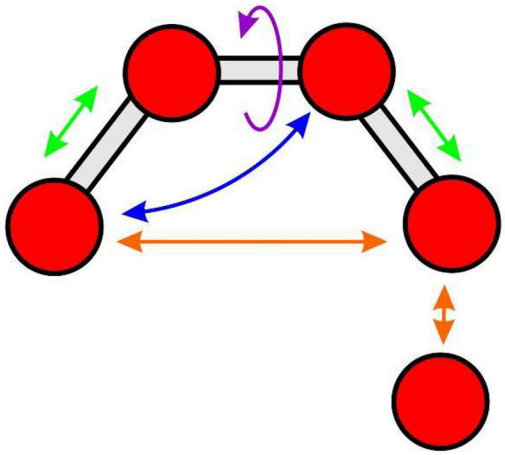

Figure 2.10. Molecular interactions, comprising intramolecular and intermolecular interactions. Intramolecular interactions consist of bond stretch (green arrows), angular bending (blue arrow), and torsion (purple arrow); intermolecular interactions are also called non-bonded interactions (orange arrows).

The total attracting and repulsing energy between biological molecules is often represented by intramolecular (e.g., molecular bond stretching, angular bending, bond torsion) and intermolecular (non-bonded) interactions (Rappé and Casewit 1997) (Fig. 2.10). Bond stretching refers to changes in molecular bond size, and energy (E_{str}) can be calculated through the total measurement of the force constant (K_b) multiplied by bond length changes (measured length, b, minus equilibrium length, b_{eq}) (Eq. 2.24).

$$E_{str} = \sum_{bonds} \left[K_b \left(b - b_{eq} \right)^2 \right] \qquad (2.24)$$

Angular bending refers to changes in the angle between two bonds, and the energy (E_{ang}) can be calculated through the total measurement of the force constant (K_θ) multiplied by bond angle changes (measured angle, θ, minus equilibrium angle, θ_{eq}) (Eq. 2.25).

$$E_{ang} = \sum_{angles} \left[K_\theta \left(\theta - \theta_{eq} \right)^2 \right] \qquad (2.25)$$

Bond torsion refers to the rotation of a molecular bond. Energy (E_{tor}) can be calculated through the measurement of the force constant (V_n), periodicity (n), torsion angle (φ), and phase angle (γ) (Eq. 2.26).

$$E_{tor} = \sum_{dihedrals} \frac{V_n}{2}[1 - \cos(n\varphi - \gamma)] \qquad (2.26)$$

For intermolecular interactions, or non-bonded interactions, the interactions are identified with van der Waals and electrostatic energies. Both formulas use a Lennard-Jones approximate model for the isotropic part of a total diatomic molecular potential (repulsion and attraction) as a function of internuclear distance, known as 6-12 potential (Band and Avishai 2013). Van der Waals interaction refers to attraction or repulsion interactions that do not stem from chemical electric bonds (non-ionic or non-covalent), making them weak and prone to disturbance. Interaction energy (E_{vdW}) can be calculated by totalling the measurements using van der Waals' parameters (A_{ij} and B_{ij}) and the non-bonded interaction length (R_{ij}) of i and j atom pairings (Eq. 2.27).

$$E_{vdW} = \sum_{nonbonded\ pairs} \left(\frac{A_{ij}}{{R_{ij}}^{12}} - \frac{B_{ij}}{{R_{ij}}^{6}} \right) \qquad (2.27)$$

Electrostatic interaction refers to interactions between two charged particles. If the particles have the same charge, the interaction is repulsive; if they have different charges, the interaction is attractive. The energy of interaction (E_{es}) can be calculated using Coulomb's law—totalling the measurements using atom i and j electric charges (q_i and q_j, respectively), dielectric constant (ε), and the non-bonded interaction length (R_{ij}) (Eq. 2.28).

$$E_{es} = \sum_{nonbonded\ pairs} \left(\frac{q_i q_j}{\varepsilon (R_{ij})^{12}} \right) \qquad (2.28)$$

From these calculated energies (Eqs. 2.24–2.28), we can acquire the total intramolecular energy (Eq. 2.29), total intermolecular energy (Eq. 2.30), and total interaction energy (E) (Eq. 2.31).

$$E_{intra} = E_{str} + E_{ang} + E_{tor} \qquad (2.29)$$

$$E_{inter} = E_{vdW} + E_{es} \qquad (2.30)$$

$$E = E_{intra} + E_{inter} \qquad (2.31)$$

Modelling for molecular mechanics—more specifically, the molecular dynamics between two molecules—can be done using software (e.g., Ascalaph Designer). In this study (**Paper I**), the analysis of molecular dynamics is used to calculate interaction energy between mudskipper-secreted mucous and ground substrates (e.g., wood), meaning the calculated energy is the intermolecular interaction energy (E_{inter}) (Eq. 2.30). If the resultant energy is positive, the

molecules repel each other; if it is negative, the molecules are attracted to each other and may aid in the mudskipper's substrate attachment.

2.3.3 Simple Robotic Modelling

The movements of a studied organism can be modelled in a simplified manner, with a joints-and-links model, using a simple robot modelling software called RoboAnalyzer, developed by Dr. Sabir Kumar Saha (IIT Delhi).

RoboAnalyzer aids in the development of simple robotic models. Its structural geometry follows the Denavit-Hartenberg (DH) parameter, and the transformations coordinate is associated with various DH parameters, including the joint offset (b), joint angle (θ), link length (a), and twist angle (α) of neighbouring links coupled by DOF joints (Denavit and Hartenberg 1955). The software enables the analysis of kinematics, utilizing revolving (R) and prismatic/piston-like (P) joints in response to the homogenous transformation matrix (HTM) (Othayoth et al. 2017).

Simulation modes of kinematics and dynamics consist of the following:

1. **Forward kinematics** means that the initial position or angle is known; the final position or angle following the simulation is what needs to be solved. The n value of DOF with $n + 1$ joints (with frame 1 attached to the base/fixed frame and frame $n + 1$ attached to the n^{th} link) is set first, followed by the DH parameters and the HTM as T_1, T_2, T_i, to the T_n (where i = 1 to n represents the frame $i + 1$ transformation with respect to frame i) (Eq. 2.32).

$$T_i = \begin{pmatrix} \cos\theta_i & -\cos\alpha_i \sin\theta_i & \sin\alpha_i \sin\theta_i & a_i \cos\theta_i \\ \sin\theta_i & \cos\alpha_i \cos\theta_i & -\sin\alpha_i \cos\theta_i & a_i \sin\theta_i \\ 0 & \sin\alpha_i & \cos\alpha_i & b_i \\ 0 & 0 & 0 & 1 \end{pmatrix} \quad (2.35)$$

   The end-effector (EE) frame HTM, relative to frame 1 (i.e. T), is now obtainable through the multiplication of the matrix Eq. 2.32 with individual transformation matrices, T_i (where i = 1 to n) (Eq. 2.33), or the robot closure equation (Bahuguna et al. 2013).

$$T_i = T_1, T_2, \cdots, T_n \quad (2.33)$$

2. **Inverse kinematics** means that a set of joint variables to achieve a desired EE configuration (also known as the task specification) is what must be solved. This can result in multiple solutions and is more complex (Bahuguna et al. 2013). In RoboAnalyzer, the EE position and orientation in the form of HTM with a 3×3 rotation matrix can be set to obtain all possible solutions (Othayoth et al. 2017).

3. **Forward dynamics** means that the value of force (or torque) experienced by the model is already known and set; the movement details (e.g., displacement value) of the model are what must be solved.
4. **Inverse dynamics** means that the movement details of the model are known and set; the force (or torque) experienced by the model, moments of inertia at individual links, and DH parameters are what must be solved (Gupta et al. 2017). The rotational inertia of a three-dimensional object can be described as a 3×3 matrix (Eq. 2.34), and the matrix diagonal is the rotational inertia around the three-dimensional Cartesian axes (I_{xx}, I_{yy}, I_{zz}); the rest are the inertial products, which are perpendicular to the main axis (Abdulghany 2017).

$$T_i = \begin{pmatrix} I_{xx} & I_{xy} & I_{xz} \\ I_{yx} & I_{yy} & I_{yz} \\ I_{zx} & I_{zy} & I_{zz} \end{pmatrix} \qquad (2.34)$$

2.4 Engineering Designs Inspired by Fish Morphologies and Behaviours

Living organisms on Earth have evolved for billions of years to thrive in their particular environment. Thus, their morphological and behavioural designs can help us to improve the performance and efficiency of engineering designs. Taking inspiration from biological designs in nature is known as bioinspiration. Mimicking, adapting, and incorporating bioinspired designs into engineering products to solve human problems is known as biomimetics (Vincent et al. 2006). There are many ways to apply bioinspiration to various products (e.g., vehicles, materials, industrial components, robots, bionic engineering). Hence, biomimetics entails observations in nature as the input, *in silico* modelling (e.g., FEM) as the process, and a resulting product as the output.

This study aims to derive mudskipper-inspired designs from observations. However, it is first necessary to learn from previous studies on fish-inspired biomimetics. The morphological and anatomical design of fish can inspire aquatic-based engineering designs ranging from minor attributes (e.g., shark placoid scale biomimetics for wing-lift improvisation by Domel et al. 2018), to full-body designs (e.g., boxfish car design by Mercedes-Benz as Daimler Chrysler; Car Body Design 2005 *cit*. Yang et al. 2019) and robotics (e.g., glass knifefish robot by Ruiz-Torres et al. 2013). Previously, McInroe (2015) from the Georgia Institute of Technology in the US modelled a mudskipper-tetrapod-inspired robot (Fig. 2.10)—a simple robot with a motorised pair of two-DOF (single joint, connected at the base; the fin moves anterior-posteriorly) pectoral fins and a two-DOF (single joint, connected at the base; the fin moves laterally) caudal fin.

Using extensive observation data, future mudskipper robots can mimic the mudskipper even more closely, making it suitable as an amphibious drone robot or model of water-land transition among fish. Mudskippers use appendage-based locomotion (Pace and Gibb 2014), specifically pectoral fins movement. The development of this robot will enable the creation of multi-phase versatility to fill the gap in robotic technology, since current robotic R&D focuses on single phase motion, e.g., aerial, aquatic and terrestrial robots.

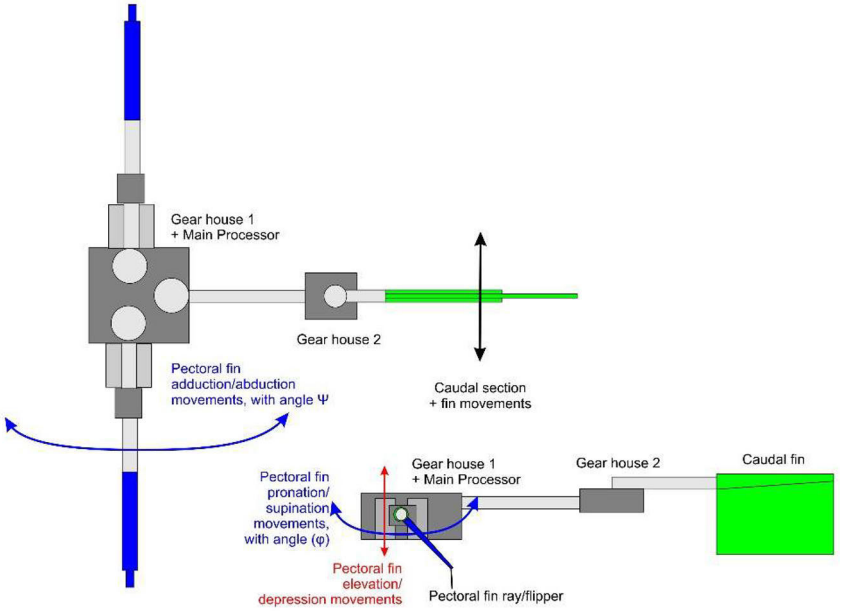

Figure 2.10. The MuddyBot (McInroe 2015) is a 3D-printed robot that simulates locomotion similar to that of an early tetrapod. It does so with an adduction angle (Ψ) of the arm between -5° and 20° with an interval of 5° and a supination angle (φ) of the flipper between -5° and 60° with an interval of 15°. This illustration is a simplification of McInroe's (2015) MuddyBot model.

3. Materials and Methods

3.1. Sampling Locations

The main species studied in this study—the dusky-gilled mudskippers, *Periophthalmus variabilis* (Eggert 1935)—was sampled from the Kaliwungu area of the Mangkang region of Kendal Regency, located west of the city of Semarang in Central Java, Indonesia. The first sample was collected between October and December 2014; the second sample was collected in June 2019.

The mudskippers with fused pelvic fins—Boddart's goggle-eyed goby mudskipper, *Boleophthalmus boddarti* (Pallas 1770)—were sampled from the coast of Rembang, Central Java, located east of Semarang. Similar to *P. variabilis*, this species inhabits the northern coast of Java. The sampling was done between October and December 2014.

The slender mudskippers, *Periophthalmus gracilis* (Eggert 1935) were sampled on the coastline of the Kulon Progo region. The non-mudskipper ornate goby, *Istigobius ornatus* (Rüppell 1830), was sampled from the Drini coastline. Both of these locations are located on the southern coast of Java in the Special District of Yogyakarta, Indonesia. Once again, the sampling was done between October and December 2014.

3.2 *In-Situ* Fish Observation and Transport Preparations

The mudskippers were prepared in three separate ways. The first sample (2014), *P. variabilis* and *B. boddarti*, was taken by capturing the fish and placing them onto transparent glass aquaria to observe their pelvic and pectoral fin movement. We also measured total body length (from the cranial snout to the tip of the caudal fin) and body weight. These mudskippers were used for the observation mentioned in Wicaksono et al. (2016) (**Paper I**).

The second sample (2014), *P. gracilis* and *I. ornatus*, was also taken by capturing the fish and placing them onto transparent glass aquaria one species at the time. The fish were captured using a fishnet with a fine, cloth-like, plastic mesh to reduce the potential harm to the fish. Following measurement, some of the fish were returned to their original habitat while some were taken for *ex-situ* observation. Along with the captured *P. variabilis* from the Kaliwungu area, these mudskippers were part of the observation mentioned in Wicaksono et al. (2017) (**Paper II**).

The third sample (2019), *P. variabilis*, was recorded on site (Kaliwungu area) using a GoPro Hero 7 Black with a high frame-per-second rate and resolution (240 FPS with 960 pixels and high efficiency video coding [HEVC]) to observe hopping behaviour kinematics. The camera was kept in a flexible handheld tripod to make it easier to capture the fish's movements. The mudskippers were poked with tree branches to prompt them to move from one side of the littoral to another. The recording was conducted in both plan view (dorsal view; *ca*. 50cm above the fish) and lateral view (side view; *ca.* 10cm from the fish). The third observation was completely *in situ*, as no mudskipper was taken to the lab and all measurements were taken on location. All of the mudskippers were returned to their habitat. Additionally, photographs of the mudskippers were taken in both plan and lateral view using a Canon EOS 550D digital camera in burst mode to ensure that a sequence of images was captured during behavioural observation. The video footage and photographs were used for the observation mentioned in Wicaksono et al. (2020) (**Paper III**).

3.3 Biomechanical Testing of Mudskippers for Attachment Strength and Preparation for *Ex-Situ* Observation

Some collected fish were kept alive (some *P. variabilis* and *B. boddarti*) and placed onto separate glass aquaria supplemented with seawater taken from their original habitat. The observation was carried out at the Laboratory of Animal Physiology and Embryology, Universitas Gadjah Mada, Yogyakarta, Indonesia. The mudskippers' resistance to pulling was measured using a calibrated spring scale (based on spring load deflection) to test suction (pulled perpendicularly from the horizontal testing surface) and friction (pulled parallel to the horizontal testing surface). The pelvic fins (fused and unfused) were then characterised to produce three-dimensional FEM designs for both pelvic fin types.

Some fish were preserved for musculature characterisation (*P. variabilis*, *P. gracilis*, and *I. ornatus*). They were then immobilized, euthanized, and later preserved in 10% formalin or 10% ethanol (separately) for each fish (i.e. one in formalin, one in ethanol).

3.4 Dissection

Dissection and anatomical observation were carried on the Laboratory of Natural Materials Technology, Åbo Akademi University, Turku, Finland. As the prepared fish bodies were already rigid, the first thing to analyse was the relationship between the pectoral and pelvic fins when they were moved (using

tweezers) to simulate anterior-posterior pectoral fin movement. Morpho-anatomical changes were observed during the simulation. The morphological values between the pectoral and pelvic fins in the body were recorded to assess the differences. The pelvic fin girdle was then isolated from the mid-ventral area to observe the skeleton and musculature. The anatomical reference for structural comparison is a study by Standen (2010) on the pelvic girdle of a trout. Afterward, in the same area, the fish body was cut transversally to assess the position of the pectoral fins and pelvic girdle relative to the lateral muscles.

3.5 Finite Element Modelling (FEM)

FEM was performed using the COMSOL Multiphysics software to conduct two analyses of the von Mises stress distribution. The first analysis used three-dimensional, simplified, single pelvic fin structures (from the radial to the ray parts) of the fused pelvic fins of *B. boddarti* and the unfused pelvic fins of *P. variabilis*. The fused fin of *B. boddarti* was 0.1mm thick at the fin ray web; its stem bone was 0.2mm thick. The unfused fin of *P. variabilis* was 0.1mm thick at the fin ray web; its stem bone was 0.13mm thick (see details in Table 3.1). The cartilaginous part and webbed connective tissue of both fin rays were modelled as elastic isotropic materials, each with an elasticity/Young's modulus of 50 MPa (Balaban et al. 2015) and a near-incompressible solid property with a Poisson's ratio of 0.49. This elasticity and near-incompressibility correspond well to fish cartilage with a low mineralization level. Each pelvic fin model simulated the effects of friction on displacement and were loaded with force of 1 N/m from the cranial direction (anterior-to-posterior or cranial-to-caudal direction) on the fin's underside. The stem bone that connects the fin to the body was fixed (zero DOF, $U = 0$). The resultant von Mises stress in the fins was later observed in Wicaksono et al. (2016) (**Paper I**).

Table 3.1. Idealised geometry of the modelled pelvic fin components of *Boleophthalmus boddarti* and *Periophthalmus variabilis*, based on direct pelvic fins, fin rays, and fin webs.

Fin ray	Length (*B. boddarti*) [mm]	Length (*P. variabilis*) [mm]
Innermost (first) ray	11	4
Second ray	10	3.5
Third ray	7	2
Outermost ray	5.5	1.1

The second analysis used a simplified, two-dimensional mudskipper cross-section with lateral muscles, two pectoral fins on each side, and a pelvic girdle in the ventral area. The distance between the pectoral fins and pelvic girdle was distinguished for each species (*I. ornatus*, *P. variabilis*, and *P. gracilis*). The forces went inward (inward compression) to the body core from the pectoral fins' lateral sides to simulate the condition of lateral body muscles during anterior-to-posterior pectoral fin movement (based on dissection information). The two-dimensional plane representing the body's cross-section is an elliptical plane for each fish. For *I. ornatus*, it was 1.15cm high and 0.9cm wide from the centre. For *P. variabilis*, it was 0.75cm high and 0.55cm wide from the centre. For *P. gracilis*, it was 1.25cm high and 0.9cm wide from the centre. The pelvic girdle muscle was also modelled as an ellipsoid at the bottom of the cross-section. For *I. ornatus*, it was 0.2cm high and 0.35cm wide from the centroid. For *P. variabilis*, it was 0.2cm high and 0.25cm wide from the centroid. For *P. gracilis*, it was 0.2cm high and 0.25cm wide from the centroid. These values were obtained through measurement and averaged for each species; the height was typically about 50% longer than the width, resulting in an elliptical shape approximation. The Young's modulus of the lateral body muscle—47 KPa—was based on a study of cod by Nesvadba (2002). The Poisson's ratio was set to that of a near-incompressible material, 0.49. The pelvic girdle muscle is notably stiffer upon dissection, as it consists of cartilaginous matter alongside normal fish muscle. Stiffness differences were noted between relaxed and contracted muscle (Butkus 1963). Unfortunately, due to a lack of available data on these fish muscles, the stiffness increase was approximated using the Reuss model formula to determine the composite Young's modulus (E_c) from the existing layers' Young's modulus (E_1 and E_2) and the layer fraction from the whole size (F_1 and F_2) (Reuss 1929; Eq. 3.1) using a fractional ratio between the pelvic plate. Muscle was set at 0.65:035 based on the cross-sectional image analysis of the fish (Young's modulus was set at 6 GPa for the fish bone and 47 KPa for the muscle using data on cod from Nesvadba [2002]).

$$\frac{1}{E_c} = \frac{F_1}{E_1} + \frac{F_2}{E_2} \qquad (3.1)$$

From the Reuss formulation, we estimated the pelvic muscle under a contracted state to be ~3 times that of the pelvic muscle under a relaxed state. Hence, the Young's modulus was 150 kPa with a Poisson's ratio of 0.49. The FEM models of the fish cross-section were discretised using quadratic Lagrangian elements, as they are high-order polynomial elements that best follow the curvature. We used plane stress formulations (Eqs. 3.2 and 3.3) with Young's modulus, E, Poisson's ratio, ν, stress, σ, and strain, ε. The orthogonal Cartesian axes are represented by the numbers 1–3. The basis for this computation formed

a system of asymmetrical sparse linear solvers (UMFPACK). We later observed displacement and stress on the pelvic girdle (Wicaksono et al. 2017; **Paper II**).

$$\sigma_{31} = \sigma_{13} = \sigma_{32} = \sigma_{23} = \sigma_{33} = 0 \qquad (3.2)$$

$$\begin{pmatrix}\sigma_{11}\\ \sigma_{22}\\ \sigma_{12}\end{pmatrix} = \frac{E}{1-v^2}\begin{bmatrix}1 & v & 0\\ v & 1 & 0\\ 0 & 0 & \frac{1-v}{2}\end{bmatrix}\begin{pmatrix}\varepsilon_{11}\\ \varepsilon_{22}\\ 2\varepsilon_{12}\end{pmatrix} \qquad (3.2)$$

3.6 Fourier Transform Infrared (FTIR) Spectroscopy

The mucous samples from *P. variabilis* and *B. boddarti* were collected by scraping the mudskippers' outer surfaces as gently as possible with a small plastic scraper to avoid causing injury to their epidermal tissue. The mucous samples were collected from the whole body surface. The mucous was removed from the scraper using a micropipette (with a 10µL tip) and placed on microtubes labelled for each species. The microtubes were then refrigerated prior to analysis. FTIR spectroscopy was performed in conjunction with attenuated total reflectance (ATR) mode at the Faculty of Pharmacy, Universitas Gadjah Mada, Yogyakarta, Indonesia. The resultant graphs were then analysed to determine the chemical constituents of the mucous for molecular dynamics analysis.

3.7 Molecular Dynamics

The simulation was performed using Ascalaph Designer with the Firefly/PC General Atomic and Molecular Electronic Structure System (GAMESS) package and electrostatic MP2/6-311+G(2d,p) method for quantum mechanical simulations. The results of FTIR spectroscopy on the mudskipper mucous and substrate material (CaCO3 to represent limestone, silica to represent sand, and cellulose, hemicellulose, and lignin to represent trees) were drawn in the software for modelling. The chemical structures were simulated under an implicit Sheffield water condition (Grant et al. 2007) with a timestep of 2.5fs in a vacuum. The united-atom force field was then optimized for the intramolecular and intermolecular interaction analyses (Case et al. 2005) (Eqs. 2.31 and 2.32 for intramolecular and intermolecular analysis, respectively, and Eq. 2.33 for overall analysis); it included harmonic potentials to model angle terms (Yang et al. 2006). We then observed the strongest interaction value for energy between van der Waals (Eq. 2.28) and electrostatic interactions (Eq. 2.29), which constituted the intermolecular (non-bonded; Eq. 2.32) interactions.

3.8 Video Observation and Analysis

The video footage from the Go Pro Hero 7 Black camera were post-processed using Adobe Premiere CS5 and VideoPad Video Editor to observe the different patterns of behavioural movements (e.g., water-hopping, land-hopping, swimming). Distances were measured using ImageJ, an image analysis software, and fish length (measured after capture) as a distance scale. The resultant data were used to model mudskipper kinematics for robotic analysis.

3.9 Simple Robotic Analysis

To generate the dots-and-sticks model of the mudskipper, Adobe Photoshop CS6 was used on still-frame images derived from the video footage using VideoPad Video Editor. We used RoboAnalyzer v. 7.4 to create simple mudskipper robot models. RoboAnalyzer displays basic analysis on a simple revolving joint (R mode) and prismatic movement (P mode) (Rajeevlochana and Saha 2011).

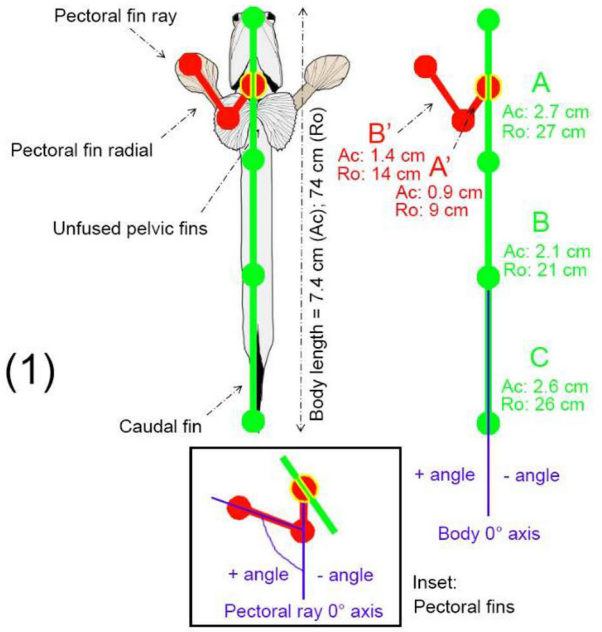

Figure 3.1. The *Periophthalmus variabilis* (from Wicaksono et al. 2016) vs. the dot-and-stick model for the body (green) and pectoral fins (red) (with three DOF for the body and two DOF for the pectoral fin): (1) A = Cranial section, B = Midsection, C = Caudal section, A' = Pectoral fin radial, and B' = Pectoral fin ray. The angle of joint (dot) deflection for the body and pectoral radial is measured through the body axial 0° axis; the deflection of the pectoral ray (inset) is measured through the pectoral ray 0° axis, which is extended from the pectoral radial. The pectoral-body joint (red dot with yellow outline) represents the pelvic girdle (pelvic fin base musculature-bone frame) area, which is set with a prismatic joint. Ac = Actual size; Ro = Robot size. (2) RoboAnalyzer robot model with three joints and three links (with link ends).

Due to RoboAnalyzer's inability to make a sensible and practical model of a smaller version of the mudskipper's body dimension, the inputs were set to be 10 times larger than their actual size (Fig. 3.1.1). This is also inspired by the earlier design by McInroe (2015), which the MuddyBot design is close to conventional drone-sized robot instead of palm-sized robot. The analysis of the mudskipper's body stances entailed mapping the point-to-point system using the *P. variabilis* figure (Fig. 3.1.2) to imitate the movements of each joint. Within RoboAnalyzer, the body was set with three DOF, or three links with three revolving joints (3R): the joint in A, the joint between A and B, and the joint between B and C. For the pectoral fins, three DOF for the pectoral-pelvic girdle (pelvic fin base musculature-bone frame) piston simulation with a prismatic (piston-like) joint and two revolving joints (hence, PRR configuration), and two DOF for the pectoral radial-ray joint simulation with all revolving joints (2R). The kinematics details were later set based on video analysis. Due to size proximity, all 3 segments were set with the same mass.

The models were later analysed under forward kinematics (i.e., known initial positions and angular orientations of the body joints, with outputs comprising the final positions and angular orientations) and inverse dynamics (i.e., looking for the force experienced by the system based on kinematical movements). The outputs are spatial data (i.e., EE displacement distance in X, Y, and Z of the Cartesian axes) and kinematics data (i.e., the connections between joint angle displacements, angular velocities, angular accelerations, and torque).

$$\omega = \theta/t \qquad (3.3)$$

$$\alpha = \omega/t \qquad (3.4)$$

Angular velocity (ω; in degrees/s) is measured in Eq. 3.3 as the angle of deflection (θ; in degrees) per unit of time (t). Angular acceleration (α; in degrees/s^2) is measured in Eq. 3.4 as angular velocity per unit of time.

$$\tau = Fr \qquad (3.5)$$

Torque (τ; in N.m) is measured in Eq. 3.5 as the multiplication of the unit of force experienced by the joint as a result of movement on the link/beam (F; in Newton, N) and the link length (r; in meters). The data outputs are represented as graphs.

4. Results and Discussions

4.1 Biomechanical Characterization

The observations enabled us to characterise the mudskipper's biomechanical details—such as substrate attachment using pelvic fins, terrestrial locomotion (i.e., crutching) assisted by the synchronised movement of pectoral and pelvic fins, water-hopping, and other behavioural kinematics (e.g., swimming)—which can serve as the basis for prospects in biomimetics and bionic engineering.

4.1.1 Pelvic Fins Flexibility and Mediated Attachment

In both orientations, be it vertical (i.e., "climbing" mode, parallel to the direction of gravity) or horizontal (i.e., perpendicular to the direction of gravity), the mudskipper's body is exposed to forces in the direction opposite to its caudal section—gravity in vertical orientation, water currents in horizontal orientation.

As mudskippers' pelvic fins are located on their ventral region and directly contact the substrate, their fin bones (ray bones, or *lepidotrichia*) must be strong enough to suspend the body. The segmented bones of the *lepidotrichia* (Genten et al. 2009) can provide additional roughness, contributing to friction and adding more resistance against the substrate. Thus, the pelvic fins may experience structural stress, requiring them to be structurally strong. Additionally, depending on the pelvic fins' morphology, they can provide either suction or attachment to the substrate.

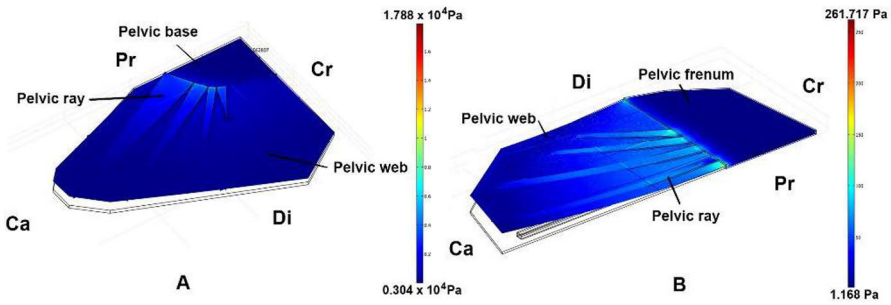

Figure 4.1. The FEM result of *P. variabilis* (A) and *B. boddarti* (B) pelvic fins under 1 N/m force exposure, demonstrating differences in the peak stress limit (i.e., maximum and minimum) of each pelvic fin of unfused and fused fins. Pelvic fin structures are based on Polgar (2010) in Fig. 6. Orientation note: Ca – Caudal (tail); Cr – Cranial (head); Di – Distal (further from central axis); Pr – Proximal (closer to central axis). Both fins are viewed from a dorsal perspective; hence,

both deformations show that the fin structures bend upward. This figure is modified from Wicaksono et al. (2016) (**Paper I**).

Based on the FEM simulation results (Fig. 4.1; Wicaksono et al. 2016; **Paper I**), the unfused fins of *P. variabilis* are able to flex four times more under the same loading condition (1 N/m) than the fused fins of *B. boddarti* (8.7μm compared to 2.0μm). This reveals that the geometrical construct of the pelvic fins of *B. boddarti* is more rigid than that of *P. variabilis*. The fin rays (the bones) of *B. boddarti* are spread across the entire web of the fins, effectively stabilising the fin structure. The fin rays of *P. variabilis* are localised to both sides of the unfused fins. The pelvic fins' rigidity in *B. boddarti* prevents the fish from having intimate contact with the substrate material surface, reducing its ability to adhere to high-incline substrates. The flexible pelvic fins of *P. variabilis* allow for closer contact; combined with the mucous secretion that improves Stefan adhesion, the fins enable the mudskipper to adhere to high-incline substrates (e.g., tree bark, rocks). In addition, at high flexion levels, the pelvic fins of *P. variabilis* experienced higher localised stress (485 Pa) than those of *B. boddarti* (61 Pa) at the tip of the longest fin ray. Nevertheless, these stress levels are relatively low, as the supporting cartilaginous material is highly elastic. The displacement level varies between the innermost and outermost fin rays on each species (in *B. boddarti*, innermost ray is 1.6μm and outermost ray is 0.22μm; in *P. variabilis*, innermost ray is 5.9μm and outermost ray is 0.8μm). The range of displacement is higher in *P. variabilis*, revealing higher deformational versatility.

From the FTIR result of two mucous samples from each mudskipper (Wicaksono et al. 2016; **Paper I**), both spectra can be identified as representing the structure of hyaluronic acid (HA) as the predominant structure, a polysaccharide composed of 1,4-glucuronic acid and 1,3-N-acetylglucosamine monomer. This aligns with the findings of Alkrad et al. (2003) and de Hoog et al. (2010). Placing the discovered structure of HA in the molecular dynamics simulations to model the mucosal biopolymer-climbing substrate interactions, the total interaction energy (van der Waals and electrostatic) of HA molecule and $CaCO_3$, followed by HA and silica, are the highest and showed attractive interactions (negative values; -266.9 kcal/mol and -160.6 kcal/mol, respectively, for HA-$CaCO_3$ and HA-silica). As for HA and plant cell constituents (cellulose, hemicellulose, and lignin), the interactions are also attracted to each other, with -50.0 kcal/mol, -71.3 kcal/mol, and -7.3 kcal/mol, respectively, for HA with cellulose, hemicellulose, and lignin. Hemicellulose is a molecule with branched structures while cellulose has a linear structure (Yang et al. 2007). The structural branching spreads the molecule, providing more interactions. Lignin interaction with HA has the lowest interaction energy, possibly due to lignin hydrophobicity. Lignin is a hydrophobic molecule (Holmgren 2008) while hemicellulose (Farhat et al. 2016) and cellulose (Khazraji and Robert 2013) are hydrophilic. When the

mudskipper comes in contact with the substrate, the secreted mucous can be highly diluted (especially if the mudskipper just climbed from the water) and/or become concentrated as the water evaporates over time. This viscosity change in the mucous may later affect the mudskipper's wet adhesion.

In term of fluid-mediated adhesion force (F_{WA}; Eq. 2.15), assuming that both mudskippers have the same HA and concentration as the mucous fluid, the mucous viscosity and fluid contact angle possessed by both *B. boddarti* and *P. variabilis* are the same. Hence, the force from surface tension (F_{ST}; Eq. 2.12), the force from Laplace pressure (F_{Lap}; Eq. 2.13), and the force from Stefan adhesion (F_{Stef}; Eq. 2.14) should be better in *B. boddarti*.

However, the unfused pelvic fins of *P. variabilis* are fully extended laterally and nearly flat on contact with the adhesion substrate (see red arrow in Fig. 4.2B2). In contrast, the fused pelvic fins of *B. boddarti* form a curve (see red arrow in Fig. 4.2A2) from the frenum (Fig. 4.2A2 compared to Fig. 4.2B2; anatomic reference: A1 and B1, a). Therefore, the contact radius is lower and the *P. variabilis* pelvic fins are more flexible; thus, the deformed fins will cover a wider substrate surface area, increasing wet adhesion for *P. variabilis*.

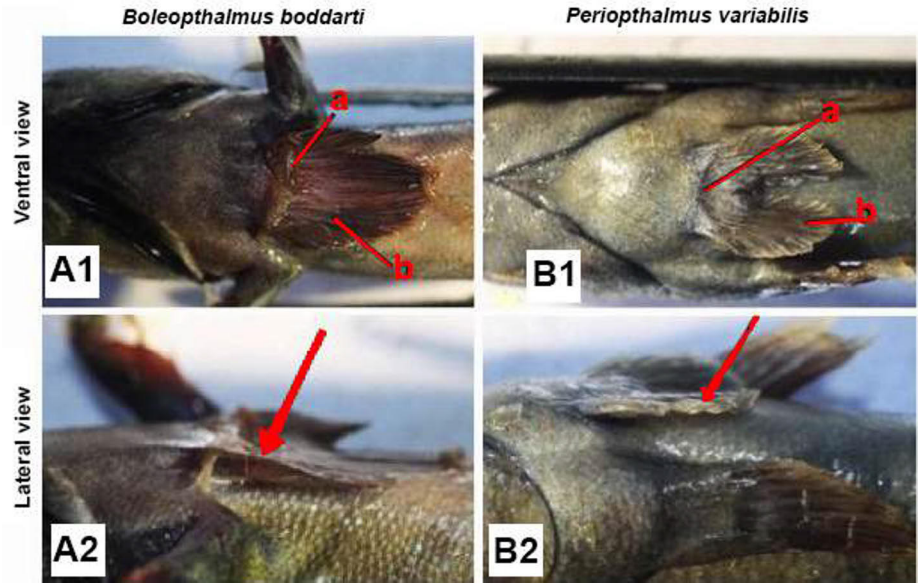

Figure 4.2. Close-up views of the pelvic fins of *Boleopthlamus boddarti* from a ventral view (A1) and a lateral view (A2) and those of *Periopthalmus variabilis* from a ventral view (B1) and a lateral view (B2). Pelvic fin anatomy: the frenum (a) and the pelvic ray (b). Red arrows indicate the pelvic fins lateral ends (Hidayat et al. 2022).

From the pelvic fins' geometry, we learned that wet adhesion is more favourable in *P. variabilis*. In *P. variabilis*, the pelvic fin-to-body area ratio is larger due to the unfused pelvic fins (0.19), in contrast to the *B. boddarti* (0.17). Thus, there is more area to cover with mucous to adhere to the substrate. Importantly, however, there are differences in body weight between the species. *B. boddarti* has a higher average mass (18.50 ± 5.41 gram) than *P. variabilis* (3.72 ± 1.54 gram), and lighter bodies can more easily be held by the force of wet adhesion against the force of gravity.

In addition to the less favourable pelvic fins for wet adhesion, the higher average of mass makes *B. boddarti* clearly less likely than *P. variabilis* to sustain adherence to high-incline substrates. Additionally, by relying solely on its pelvic fins, *P. variabilis* is able to stick to glass aquaria without extending its pectoral fins (Fig. 4.3). Pelvic fins constitute static sticking surfaces while pectoral fins serve as dynamic sticking surfaces that propel the fish forward while still providing additional Stefan adhesion.

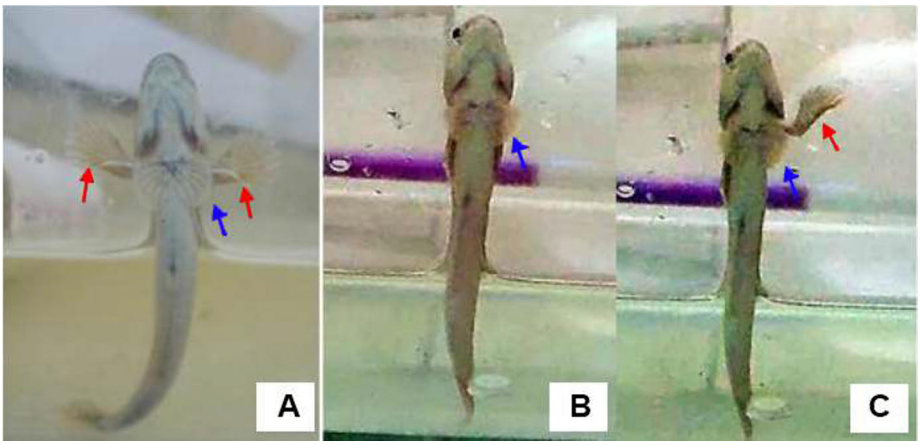

Figure 4.3. *P. variabilis* adheres to the aquarium glass with both pectoral and pelvic fins fully extended (A), with only pelvic fins extended (B), and with pelvic fins and a single pectoral fin extended (C). Blue arrows indicate the pelvic fin rays while red arrows indicate the pectoral fin rays. Figure modified from Hidayat (2015) and used with permission.

4.1.2 Pectoral Fins vs. Pelvic Fins: Terrestrial Locomotion

There are pectoral fin anatomical differences that help the mudskipper grip the substrate. The pectoral fins of *B. boddarti* have a much smaller radial size ratio than those of the *P. variabilis* (Hidayat 2015; Fig. 4.4). With a larger radial size extended from the body to support the fin rays, the pectoral fins of *P. variabilis* are similar to features of the early tetrapod aquatic-terrestrial transition among

ancient lobe-finned fishes (Kutschera and Eliott 2013; Okamoto et al. 2018), as the extended pectoral fins provide more contact with the substrate surface and possibly enhance the grip features. The pectoral fins with smaller radials in *B. boddarti* are more suitable for an aquatic lifestyle. This is supported by the fact that the feeding behaviour of *P. variabilis* is more adapted for hunting active prey for food, such as small arthropods (Swennen et al. 1995, referring to the closest relative *P. novemradiatus* F. Hamilton). *B. boddarti* engages more in grazing for substrate microalgae (e.g., diatoms) (Swennen et al. 1995; Tran et al. 2020).

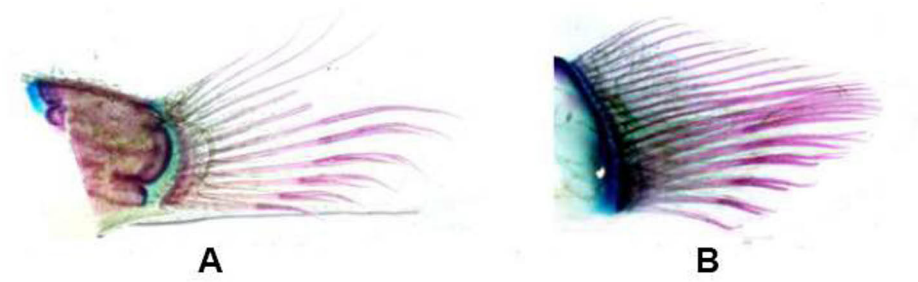

Figure 4.4. Pectoral fins of *P. variabilis* (A) and *B. boddarti* (B) (Hidayat, 2015; used with permission).

The smaller mudskipper, *P. gracilis*, which has unfused pelvic fins, is also able to adhere to glass aquaria. With synchronised pectoral fin movement, both *P. variabilis* and *P. gracilis* move terrestrially through a "crutching" locomotion, as detailed by Harris (1960), which used *Periophthalmus koelreuteri* Pallas as the mudskipper specimen. Pectoral fins equipped with large pectoral radii work as a crutch that moves the fish forward (Gibson 1986). To stabilise the more caudally oriented body part, the pelvic fins must be extended and act like a pad (Sayer 2005). It is fair to assume that they function similarly to the hind limbs of a tetrapod. However, unlike in tetrapods, where the pelvic bones are connected to the vertebral column, the pelvic fins' bone frame and musculature are completely separate from the core body.

Along with the mudskippers with unfused pelvic fins (*P. variabilis* and *P. gracilis*), we examined the ornate goby with fused pelvic fins, *Istigobius ornatus*. The objective is to compare terrestrial locomotion (semiaquatic testing was done on *I. ornatus*, as it is a fully aquatic fish) in an aquarium and the body anatomy for pectoral-pelvic fin connections.

During the aquarium testing (Wicaksono et al. 2017; **Paper II**), the mudskippers moved their pectoral fins in manners identical to those exhibited while crutching (Fig. 4.5B and C). The *I. ornatus* moved its pectoral fins in a rowing motions with its large pectoral rays stroking in lateral-backward locomotion and some areas of the fin rays making contact with the substrate (Fig. 4.5A).

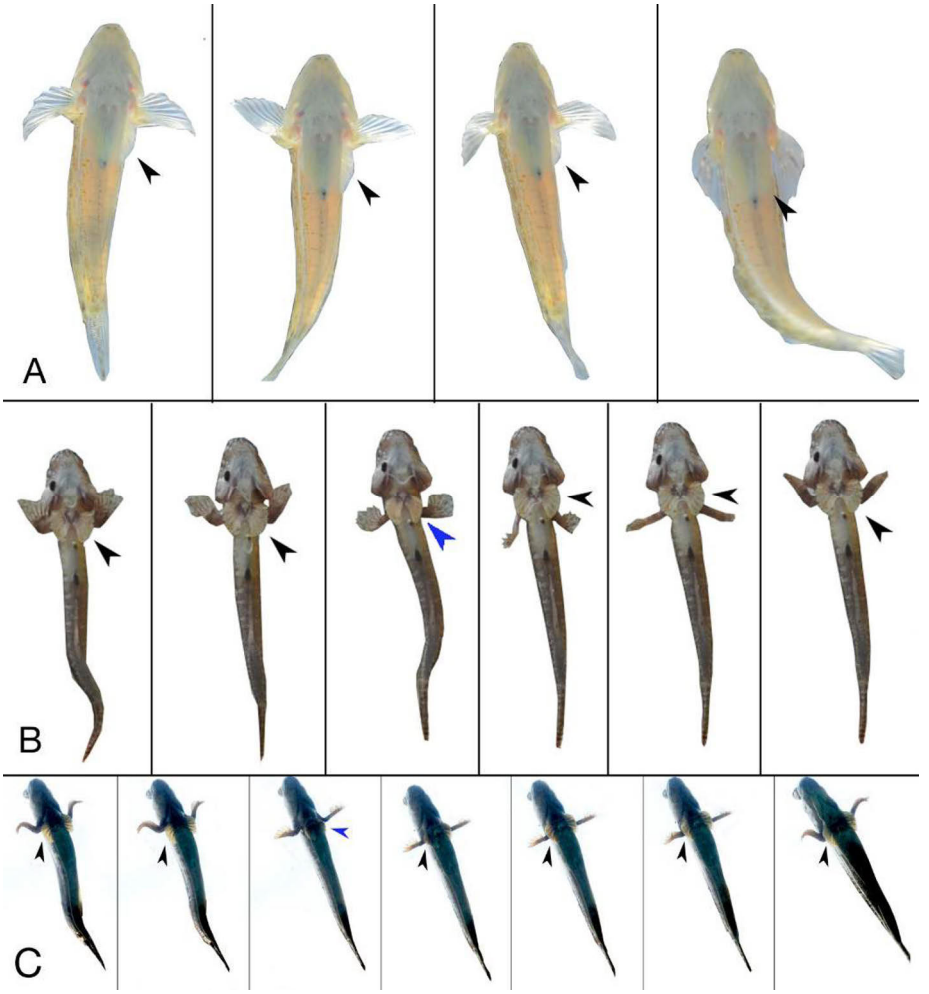

Figure 4.5. Pectoral fin vs. pelvic fin movement in *I. ornatus* (A), *P. gracilis* (B), and *P. variabilis* (C). The black arrowheads point to the pelvic fin locations in contact with the substrate with unchanged fin geometry; the blue arrowheads point to the timeframe at which the pelvic fins are retracted. These images are featured in Wicaksono et al. (2017; **Paper II**). Figure 4.5C was taken and modified with permission from Wicaksono et al. (2016; **Paper I**).

Regarding the mudskippers' pelvic fins, when the pectoral fins crutched backwards, the pelvic fins were deployed to the substrate to laterally stabilise the body (Fig. 4.5B and C). For comparison, when the pectoral fins of *I. ornatus* rowed backwards, the pelvic fins extended, potentially stabilising the body in a single-pad form (Fig. 4.5A). According to Thomson (2019), the mudskipper's crutching locomotion—also referred to as ambipedal progression—can be viewed as a form of pentapedalism (five appendages), as in kangaroos. This is because the five appendages can be represented by two pectoral fins, two pelvic

fins, and the caudal section of the body. The fishes with fused pelvic fins can vary in the degree to which the pelvic fins extend from the body axis in contact with the substrate. Therefore, in the case of *I. ornatus* and *B. boddarti*, where little to none of the pelvic fins' area contacts the substrate, both species can be pseudo-pentapedalism or tripedalism, respectively.

The pelvic fins are connected to the pelvic girdle, where the musculature is bound to the pelvic disc bones that constitute a single frame (Standen 2010). However, unlike tetrapods, where the pelvic bones are connected to the vertebral column, fish pelvic bones are loosely connected by lateral muscles (Don et al. 2013). Adductor muscles constitute the main locomotor to extend the pelvic fin rays (Standen 2010). However, in pushing the pelvic fins further ventrally to make contact with the substrate, this study (Wicaksono et al. 2017; **Paper II**) reveals that the inward pressure from both lateral directions caused by the pectoral fin radials' backward strokes may instigate the piston-like movement of the pelvic fins in the ventral direction, contacting the substrate without using multiple musculatures, as with tetrapods, resulting in a low-energy effort.

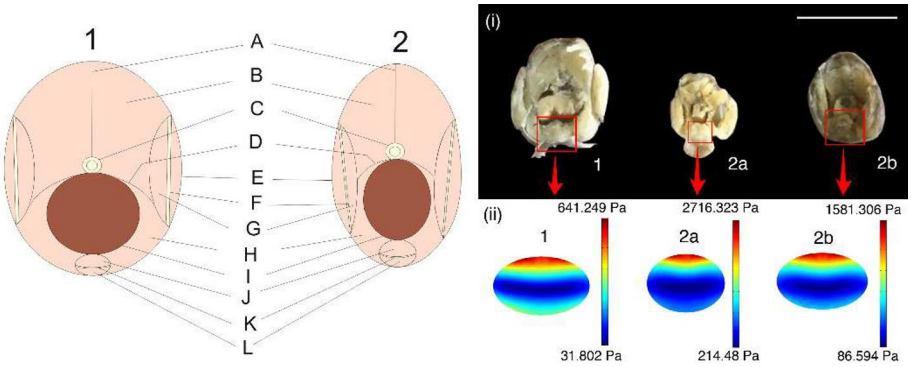

Figure 4.6. The anatomical illustration (left) and actual cross-sections (right; i) of the *I. ornatus* (1) and the mudskippers (*P. gracilis*, 2a; *P. variabilis*, 2b). Under lateral pressure during pectoral radials' backward strokes, we can see the FE-generated model of von Mises stress experienced by the pelvic discs of each species (right; ii). This figure is featured in Wicaksono et al. (2017; **Paper II**).

To provide evidence using FEM, the cross-sections where the body axis intersects with the pectoral radials in both the lateral area and pelvic fin girdle disc of both mudskippers (*P. variabilis* and *P. gracilis*) and *I. ornatus* are modelled based on the dissection characterisations. The results show that, in both mudskippers, which possess more ventrally oriented pectoral fins (compared to the laterally oriented pectoral fins of *I. ornatus*), the inward lateral pressure from

the pectoral radials presses the lateral muscle downward, resulting in the ventral displacement of the pelvic discs (Fig. 4.6; right 2a and 2b). The stress experienced by the pelvic disc of *I. ornatus*, however, is two-directional (dorsal and ventral) and mutually nullifying (Fig. 4.6; right 1). Despite the dorsal-originated stress being slightly larger than the ventral-originated stress, the resultant pressure only pushes the pelvic disc of *I. ornatus* a tiny distance ventrally, compared to the mudskippers' pelvic discs.

In this way, the pectoral fins and unfused pelvic fins of the mudskippers work in a sequential but antagonistic manner. As the pectoral fins stroke backward and loosen contact with the substrate, the pelvic fins are deployed to stabilise the body in a low-energy, piston-like deployment to limit the chance of the body tumbling laterally.

4.1.3 The Mechanics of Hopping

As an escape mechanism, the mudskipper can hop. The land-hopping kinematics of the mudskipper have been characterised by Swanson and Gibb (2004) on *P. argentilineatus* (Valenciennes, 1837). Water-hopping is the newest mode of hopping to be characterised in this study (Wicaksono et al. 2020; **Paper III**).

Figure 4.7. *P. variabilis* performs a terrestrial hop, depicted in a sequential timeframe. The body configuration aligns with the description by Swanson and Gibb (2004).

The land-hopping behaviour characterised by Swanson and Gibb (2004) and observed in the field during this study (Fig. 4.7) is initiated by the mudskipper laterally bending its caudal section to be parallel to its mid-to-cranial section, forming a J-shape. The mudskipper then rapidly pushes against the substrate underneath by rapidly straightening its caudal section in a lateral-ventral move (sideways in the direction of the substrate) that functions as a spring to bring the entire body airborne (i.e., in the cranial direction). The rapid caudal push against the ground provides enough kinetic energy to move the mudskipper into the air.

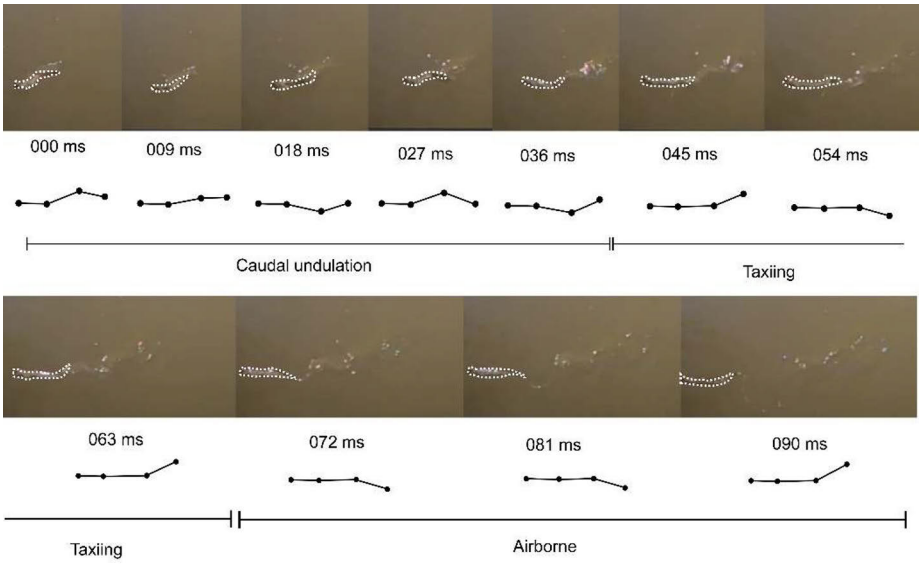

Figure 4.8. Mudskipper water-hopping sequence. Featured in Wicaksono et al. (2020; **Paper III**).

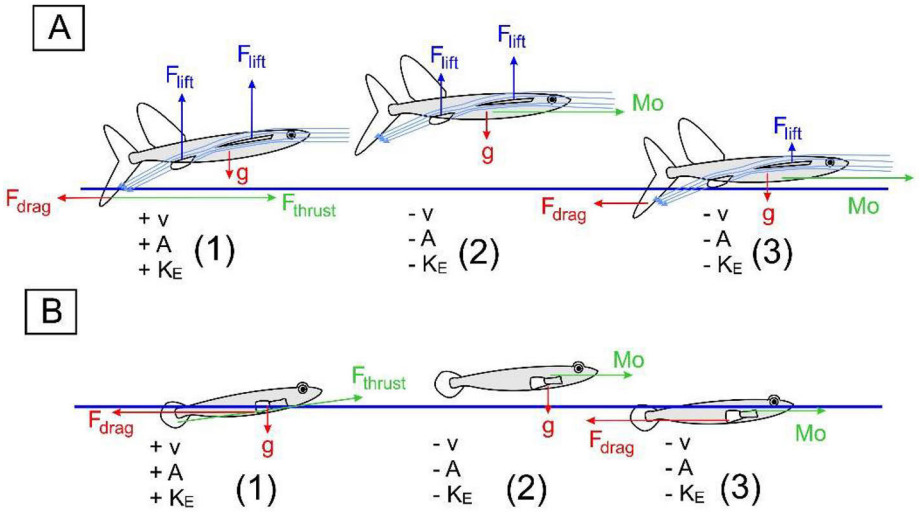

Figure 4.9. Comparison of the take-off and airborne kinematics in the flying fish (A) and the mudskipper (B). The flying fish, due to its enlarged pectoral and pelvic fins, can produce lift (F_{lift}) through the airflow Kutta condition (airflow separation on the fin/wing leading edge and merging on the back) in addition to using momentum (Mo) to counter gravity (g). The mudskipper, however, relies on its head for momentum redirection to go airborne. The take-off is essential to building up velocity (v), as it accelerates (A) and generates kinetic energy (K_E)

through cyclic caudal fin movements (F_{thrust}) to counter the drag (F_{drag}) used for getting airborne.

In the water, however, this caudal spring action is not effective, as the water density is too low to generate enough kinetic energy (K_E; Eq. 4.1). To compensate, the mudskipper (as observed in **Paper III**, *P. variabilis*) uses rapid, cyclic caudal movements to build velocity and get airborne (Fig. 4.8). This pre-hopping take-off locomotion is quite similar to the flying fish's pre-gliding, as described by Davenport (1994) (Fig. 4.9). Of course, there are differences. The first difference is that the flying fish's caudal fins are heterocercal (one lobe is bigger) (Fish 1990) while the mudskipper's caudal fins are homocercal (lobes are equal in size). The second difference is that the flying fish extends both of its paired fins (pectoral and pelvic) during take-off to provide the Kutta condition and bring the flying fish into the air (Park and Choi 2010). This makes the flying fish's pectoral fins function like airplane wings and the flying fish's pelvic fins function like the aircraft elevator (horizontal stabilizer). In contrast, the mudskipper retracts both of its paired fins. The elongated caudal fin lower lobe in the flying fish is advantageous for maintaining contact with the water surface while the fish is partially gliding in the air. The third difference is that, for hopping, the mudskipper takes off using a short path while the flying fish takes off using a long path. The airborne periods are also different, as the flying fish glides for a much longer time and a much longer distance than the mudskipper.

$$K_E = \frac{1}{2}mv^2 \qquad (4.1)$$

Upon landing, the mudskipper can proceed to the next taxiing sequence to generate more kinetic energy and cover its loss (K_{E_loss}; Eq. 4.2). The generation of kinetic energy can be measured per unit of distance ($K_E(d)$, d is the distance, Eq. 4.3). This replenished energy is required to enable the mudskipper to water-hop again and repeat the process (Fig. 4.10A). Alternatively, if there is remaining kinetic energy, it can bounce its body off of the water surface and go airborne once again (Fig. 4.10B). The depiction of energy consumption in Fig. 4.10 is an idealised version. From the acquired kinetics (Fig. 4.11), kinetic energy per unit of distance (Fig. 4.11A) in a short water-hopping sequence appears to increase for each consecutive hopping cycle (taxiing and airborne). This shows that momentum is generated more effectively after taxiing for the next airborne ascent. However, no fixed pattern is observable in the long sequence and bouncing kinematics. As long-sequence water-hopping and bouncing require long periods of kinetic energy usage to complete the process, the mudskipper may adjust its distance to optimise energy usage.

$$K_{E\_loss} = \frac{K_{E_{in\ the\ air}}}{K_{E_{in\ the\ water}}} \qquad (4.2)$$

$$K_E(d) = K_E/d \qquad (4.3)$$

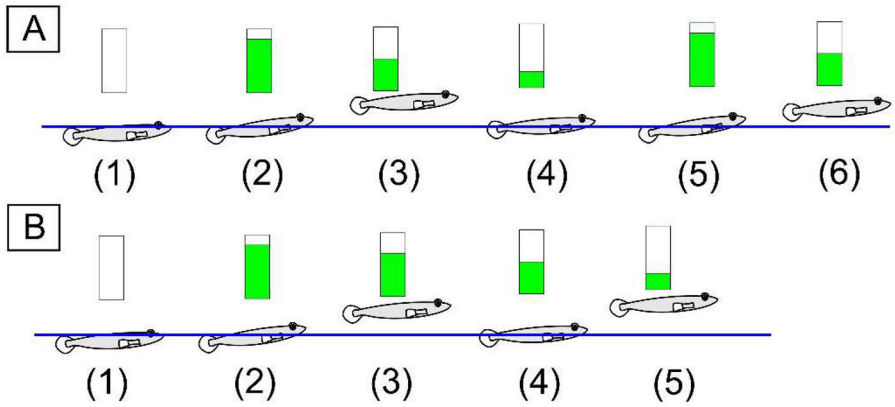

Figure 4.10. Visualisation of the kinetic energy (green bar) hypothetically possessed and used by the mudskipper during water-hopping (A) and water-bouncing (B) under ideal conditions. The green energy bars are not scaled, as they merely represent energy usage during hopping. Sequence kinematics: initial condition of taxiing (1), late taxiing stage (2), airborne (3), and landing (4). It can proceed to taxiing again (5A) to generate more kinetic energy and go airborne again (6) or it can use its remaining kinetic energy to bounce just after making contact with the water surface (5B).

The kinetic energy loss (K_{E_loss}; Fig. 4.11B) in short water-hopping sequences occurs during the air-to-water transition. During long sequences and bouncing, most loss occurs when the fish makes contact with the water. Unlike normal water-hopping, the mudskipper experiences less hydrodynamic drag because it does not require taxiing.

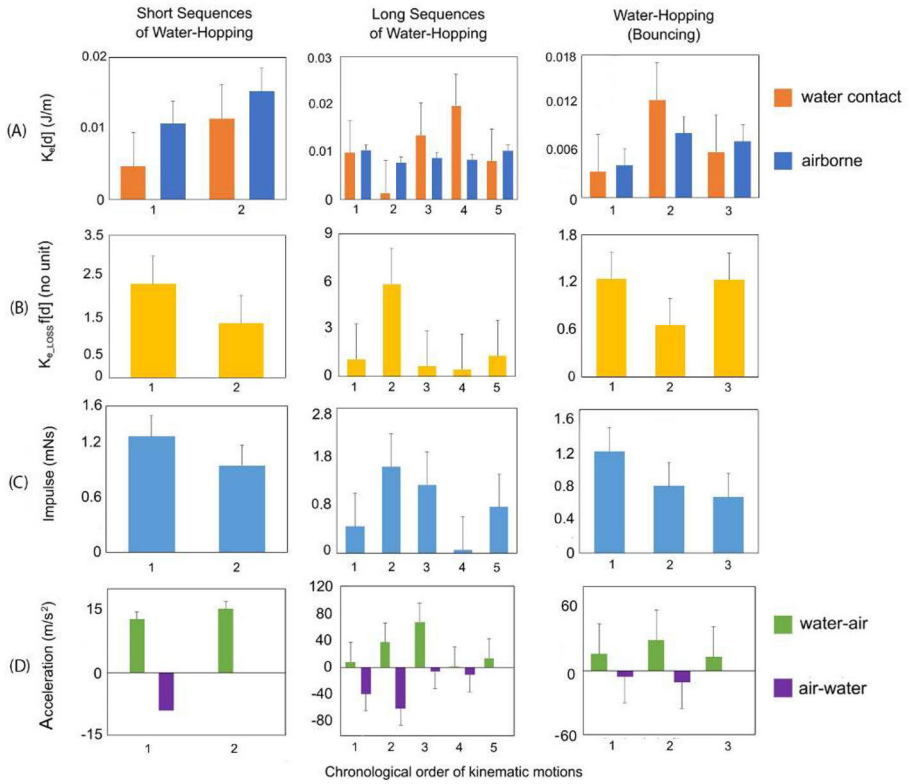

Figure 4.11. The water-hopping kinetics. Featured in Wicaksono et al. (2020; Paper 3).

The impulse (J; Fig. 4.11C) in short water-hopping and bouncing sequences shows a gradual loss of momentum from the first to last hop. However, during long hop sequences, the values are largely random. This is possibly due to the mudskippers attempting to optimise their energy usage. Acceleration (A; Fig. 4.11D) in all cases exhibits the same pattern: the mudskippers accelerate during the water-to-air transition due to taxiing and decelerate during the air-to-water transition due to hydrodynamic drag. However, we suspect that the hydrodynamic drag during bouncing is minimised by minimal contact with the water surface.

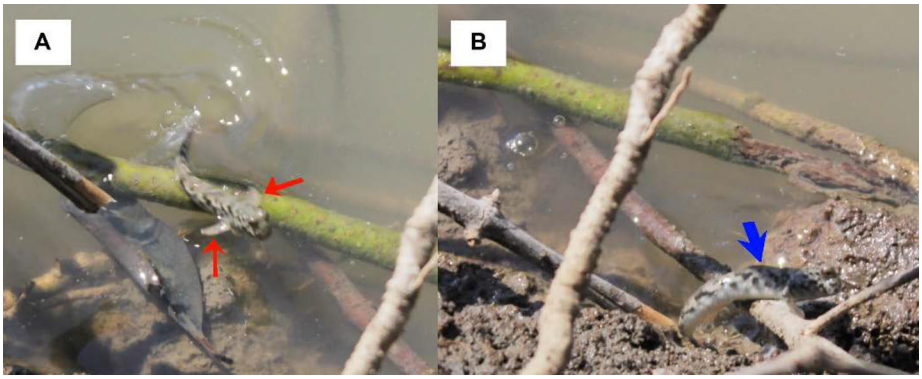

Fig. 4.12. Short hop to land from the water, with pectoral fins (red arrows) extended (A) before the mudskipper hits land (B). These images do not have a timeframe because they were taken on a digital camera.

At the end of the water-hopping sequence, the mudskipper can hop to a solid substrate (e.g., land, tree root, etc.) if it is reachable by hop. Alternatively, if the substrate is particularly close, the mudskipper can simply use its momentum to slide across the water surface. The most noticeable behaviour kinematic appeared during the final landing step (when the trajectory of the body is close to the water or solid substrate)—the mudskipper extends its pectoral fins (Fig. 4.12). Presumably, this slightly slows the landing speed to reduce the impact force and distribute the landing stress while more effectively gripping the substrate upon contact.

4.1.4 Other Behavioural Kinematics and Features

There are many other recorded behaviours in this study on *P. variabilis*, such as swimming and other hopping-related behaviours (Fig. 4.13). Through field observations, the mudskipper has been identified as a carangiform-type swimmer (Fig. 4.13F; consistent with Budi et al. 2018). This is a BCF type of swimming wherein two-thirds of the total body section (relative to the cranial area) to the caudal fins serves as the cyclic, undulatory locomotor to propel the fish forward (Sfakiotakis et al. 1999). Unlike hopping and crutching, swimming is rarely observed; it is assumed to be an energy-saving method of aquatic locomotion, as the mudskipper (*P. variabilis*) largely stays on muddy soil when undisturbed. Only after being disturbed (in this study, poked with a stick) does the mudskipper swim to adhere to an underwater substrate (Fig. 4.13A). While swimming, the mudskipper can stand still or move forward by sliding as a form

of low-energy movement to either go forward in the body of water (Fig. 4.13C) or move toward a solid substrate on its path (Fig. 4.13E).

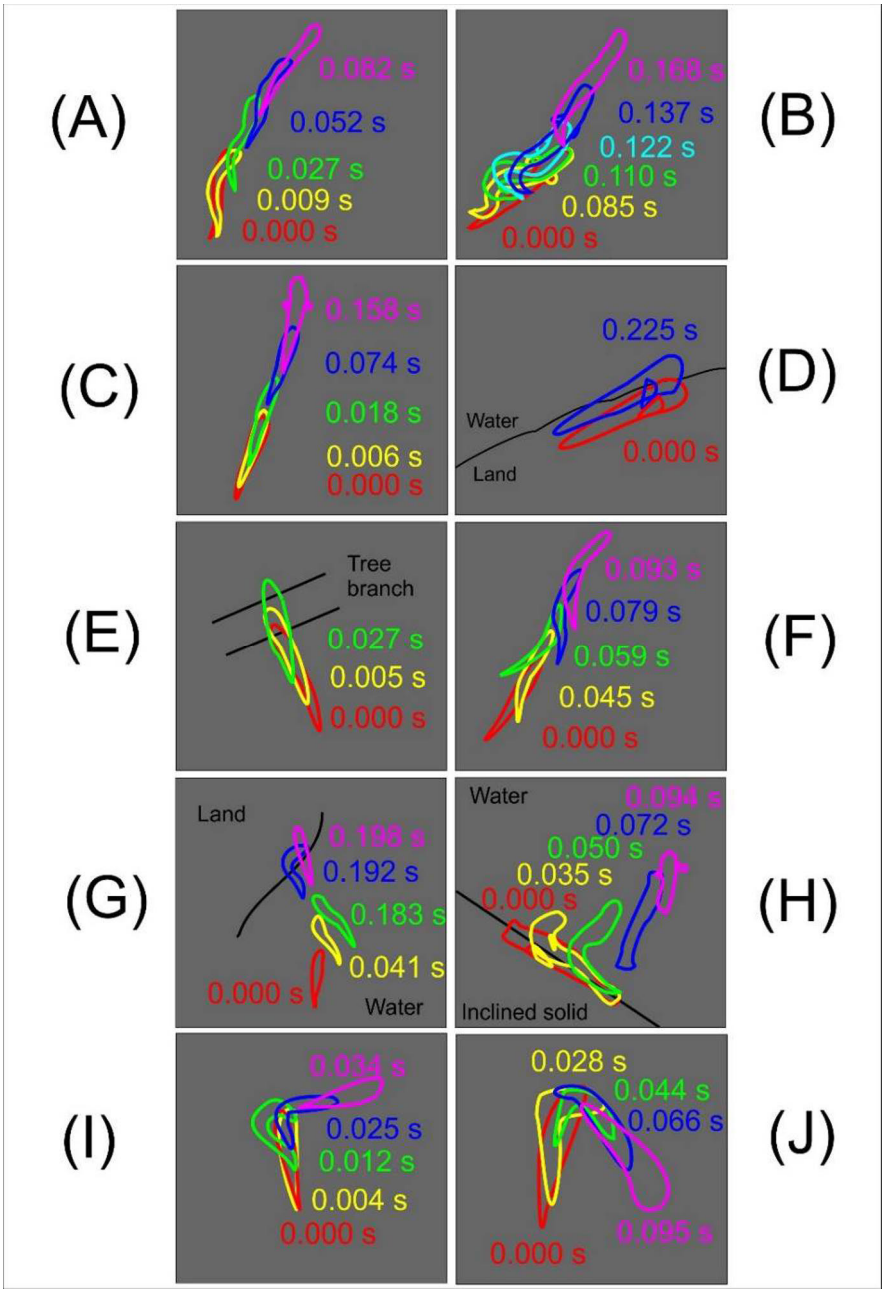

Figure 4.13. Additional behavioural kinematics of the mudskipper (*P. variabilis*): diving (A), land-hopping (B), forward sliding on the water surface (C), sideways sliding from solid substrate to water (D), forward sliding from water to solid substrate (E), swimming in carangiform type (F), short taxiing to solid substrate

from water (G), hopping to water from an inclined solid substrate (H), changing the taxiing direction (I), and making a U-turn while taxiing (J). Featured in Wicaksono et al. (2020; **Paper III**).

The ways in which the mudskipper hops and taxis are varied. From land or a horizontal solid substrate, the mudskipper can escape by land-hopping (Fig. 4.13B) to water or another solid substrate area. Alternatively, it can simply slide to water from a solid substrate (Fig. 4.13D). Additionally, prior to water-hopping or moving to another location connected by a body of water, the mudskipper can change its direction by bending its headfirst followed by the rest of its body (Fig. 4.13I) or making a U-turn in (Fig. 4.13J) while still performing the cyclic caudal movement, as in normal taxiing.

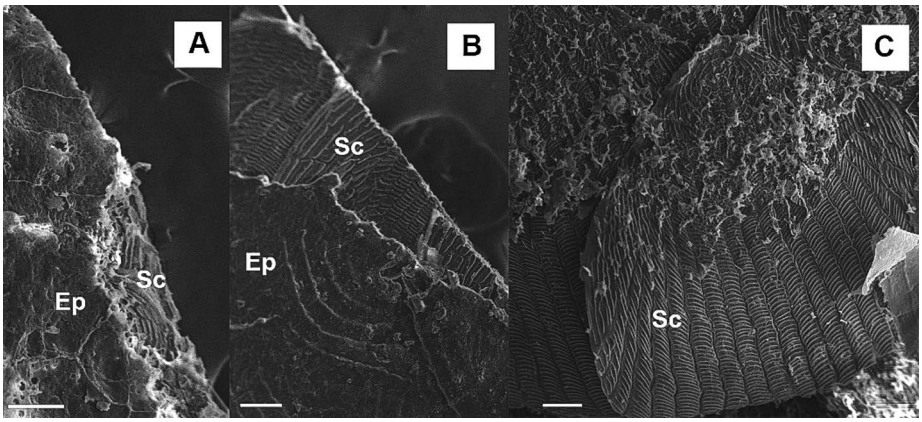

Figure 4.14. SEM images of embedded scales from the ventral, abdominal area of *P. variabilis* (A) and *P. gracilis* (B), compared to exposed scales from the same area of *I. ornatus* (C). Note: Ep – epithelial layer; Sc – scale plate. Scale bars = 100 μm.

Mudskippers are highly adapted to the terrestrial environment. Their pectoral-pelvic fin pairs are adapted for crutching on a solid substrate, and their bodies are strong enough to support land- and water-hopping and their derivative kinematics. Under normal circumstances, it is not impossible for the terrestrial locomotion to damage the fish integumentary layer (i.e., the scales). However, a minute observation under an electron microscope revealed—in line with Park (2002)—those mudskippers (P. variabilis and P. gracilis) have embedded scales under their skin layer, in contrast to most fish, whose scales are commonly exposed (Fig. 4.14). As the epithelial layer of the skin is highly vascularised among mudskippers for air-breathing, the scales underneath the skin possibly contribute to the protection of muscles or serves as a vestigial organ from the mudskipper's aquatic ancestor. It appears that *P. variabilis* and *P. gracilis*, as with *I. ornatus*, have cycloid scales, meaning they have a growth ring structure formed during fish growth (Esmaeili et al. 2007) and comprising a

hydroxyapatite and calcium carbonate outer layer and a fibrous collagen inner layer (Helfman et al. 1997 *cit*. Garrano et al. 2012). The combination of a stiff, mineralised outer layer and an organic inner layer may provide the body with strong, elastic armour. However, as mudskippers are terrestrial fishes, the scales are generally exposed to the solid substrate, making them vulnerable to scratches and impacts. Therefore, the concealment of the mudskipper's cycloid scales under its mucous-coated skin layer gives its body an extra layer of protection.

From all of the mudskippers' unique morphological, behavioural, and kinematical adaptations, there are many things we can learn to improve engineering designs, especially for adhesive and attachment features. These bioinspirations can be turned into a directly designed or abstracted (philosophical) design of biomimetics and bionic engineering.

4.2 Concepts of Bioinspired Designs Based on The Mudskippers

4.2.1 Biomimetics

Many things can be learned from the biomimetic design of mudskippers, from the durable sticker design to the protective clothing.

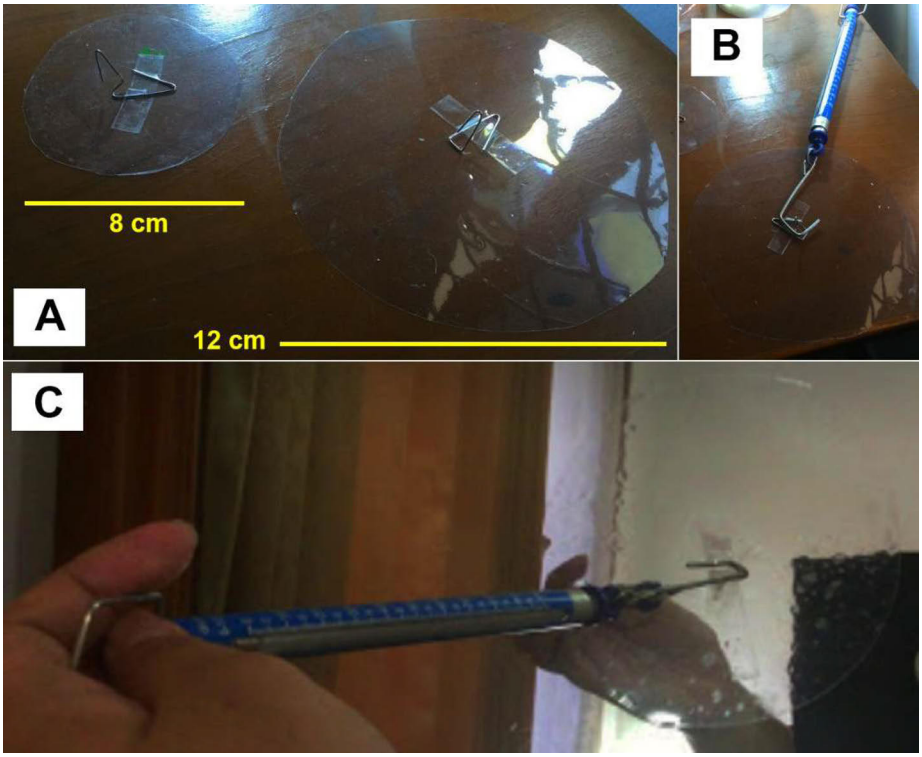

Figure 4.15. Thin flat plastic used to test Stefan adhesion with two different sizes (d = 8 cm / r = 4 cm; d = 12 cm / r = 6 cm) (A). The testing was conducted using a spring scale on both a wooden surface (B) and perfectly flat glass (C).

A Stefan adhesion-supported sticker can be made with inspiration from the ventral surface features of the mudskipper (Fig. 4.15). Testing with a plastic sheet with a diameter of 8 cm and water as the mediation fluid, the adhered plastic sheet can sustain a minimal load (close to 0 N on the spring scale) on a wooden surface and 2.2 N on a mirror surface. With a larger diameter of 12 cm and water as the mediation fluid, it can sustain an even larger load—5.9 N on a wooden surface and 7.9 N on a mirror surface. Stefan adhesion-mediated stickers use viscous fluid instead of adhesive polymers, which bind once the solvent has completely evaporated (Kuusipalo 2008). The result is that the two surfaces stick together permanently. In comparison, Stefan adhesion does not result in a permanent bind; it allows for forward and sideways movement, just like mudskippers' pectoral fins (see Fig. 4.3). This can be applied to non-permanent stickers for flat wood, mirror/glass, or ceramics surfaces or to a mudskipper-like moving robot that can adhere to inclined and vertical substrates. To note, however, this single flat plastic does not represent the fused pelvic fins of *B. boddarti* as there are gap areas in the fin-substrate contact interface that minimize the adhesion. Instead, it represents *P. variabilis* unfused pelvic fins that

are perfectly flexible and flat, enabling a full contact to the substrate with larger area, thus facilitating Stefan adhesion more effectively.

Figure 4.16. The design of a bulletproof vest (A), with the outer layer (Ou) and inner layer (In) made of kevlar and the core material (Co) made of steel, titanium, or bulletproof ceramics (B). Vest belong to Ganesh Aji Wicaksono, image was taken by himself and used with permission.

The concealed scale integument of the mudskipper (Fig. 4.14) can serve as a potential model for an elastic bulletproof armour design. One existing bulletproof vest design uses a three-layered protection system (Fig. 4.16). The outer and inner linings of the vest are made of a strong, bulletproof polymer mesh, such as kevlar. The core layer, which consists of a solid plate to further limit bullet damage, can be made of steel, titanium, or strong ceramics. Inspired by the mudskipper's elastic skin and cycloid scales, more elastic bulletproof vests could be designed to enable wearers to be more agile. While the outer and inner linings could still be made of kevlar, the core layer could be made from a more elastic material. For example, the reinforced polyampholyte hydrogel developed by Hokkaido University has extreme toughness, high tear strength, high tensile modulus, and low bending modulus (King et al. 2015).

4.2.2 Concepts of Mudskipper for Bionic Design

P. variabilis, the mudskipper in this study, is able to stick to aquaria with only its pelvic fins extended (Fig. 4.3). Paired with a concept from the biomimetic Stefan adhesive sticker (Fig. 4.15), we can achieve the design of a simple surface-adhering small robot. One example of this design is a controllable adhesive climbing robot with magnetorheological fluid (MRF), as studied by Wiltsie et al. (2012), the viscosity of which is controlled by the given magnetic field (Fig. 4.17). The robot was able to stick on a vertical board and 150 grit sanding cloth. Using

MRF, the robot maintained a sustained shear at 7.6 kPa. Without MRF, the robot slid at a 45° inclination angle with stress at 0.96 kPa. On an inverted glass sheet, it exhibited adhesion stress at 7.6 kPa.

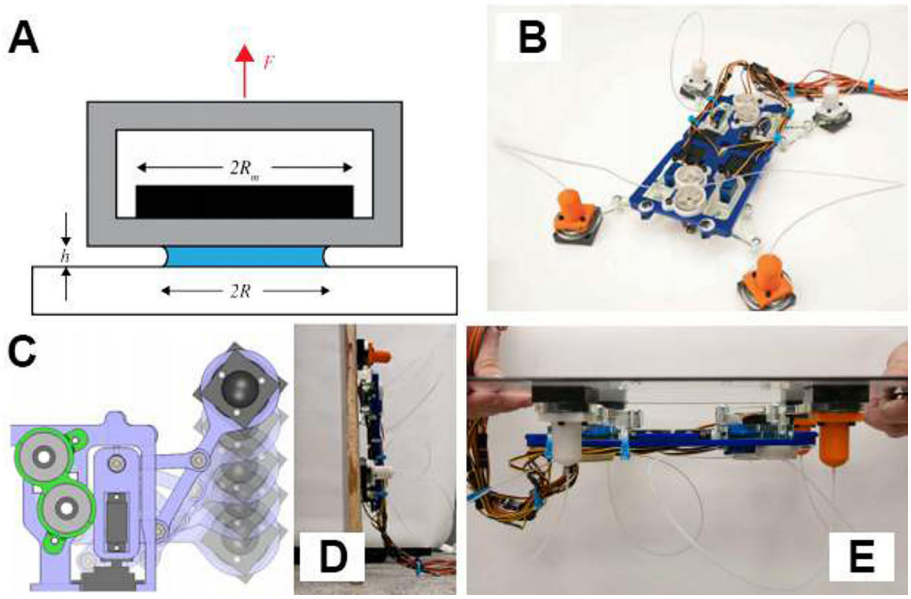

Figure 4.17. Design of a controllable surface-adhering robot with magnetorheological fluid, exhibiting Stefan adhesion on an area (with R radius and h separation distance) with magnetorheological fluid controlled by a cylindrical magnet with a certain radius (R_m), then pulled with force from its perpendicular direction (F) (A). The robot design (B) and its foot during a stepping action (step = 10 cm) (C). The robot was tested on a vertical (D) and inverted horizontal surface (E). Photos were taken from Wiltsie et al. (2012) and re-arranged. Copyright © 2012, IEEE.

McInroe (2015) designed and tested MuddyBot, a robot bioinspired by mudskippers and ancient tetrapods. This design focused on fish propulsion driven by pectoral fins and assisted by the caudal body to exert additional force. Each fin was modelled with a flipper. The MuddyBot's pectoral fins move like paddles, with the proximal part connected to the motor with only 2 DOF: one immobile part connected to the adductor motor and another that rotates like a paddle. The body component has 2 DOF as well, with one that represents the static cranial area and one that represents the laterally moving caudal region. The pectoral fins also have 2 DOF: one that represents the fin radial section and one that represents the fin web. The MuddyBot was tested in a bed of poppy seeds to simulate the muddy condition of the estuarial water bank. The bed inclination was set to 0°, 10°, and 20°. The pectoral fins could swing (adduction movement) at an angle between -5° and 20° with an interval of 5°. The pectoral

fins could also supinate to act as paddles at an angle between -5° and 60° with an interval of 15°. The MuddyBot employed its caudal body (flipper) to aid in forward movement to a greater degree as inclination increased. This is due to the decrease in the effectiveness of the pectoral fins during locomotion.

Inspired by the MuddyBot, we can achieve an even more advanced design, the MudskipperBot, with RoboAnalyzer (see Fig. 3.1 for the model), using the video observation data to model the crutching, land-hopping, and water-hopping movements. However, mimicking water-hopping will require more complex modelling in order to develop greater fin efficiency for taxiing.

Mimicking the crutching of *P. variabilis* was achieved by tracing the central lines and movement joints of the fish using the images from Wicaksono et al. (2016; **Paper I**; Fig. 4.18) to make a 3-DOF joint system. The cranium section was set to 0.027m, midsection was 0.021m, and caudal section was 0.026m. All sections were set with equally 1 g of weight each despite the size difference, judging that both mid and caudal section in actual fish are packed with internal organs, making it heavier despite the length proportion of each section.

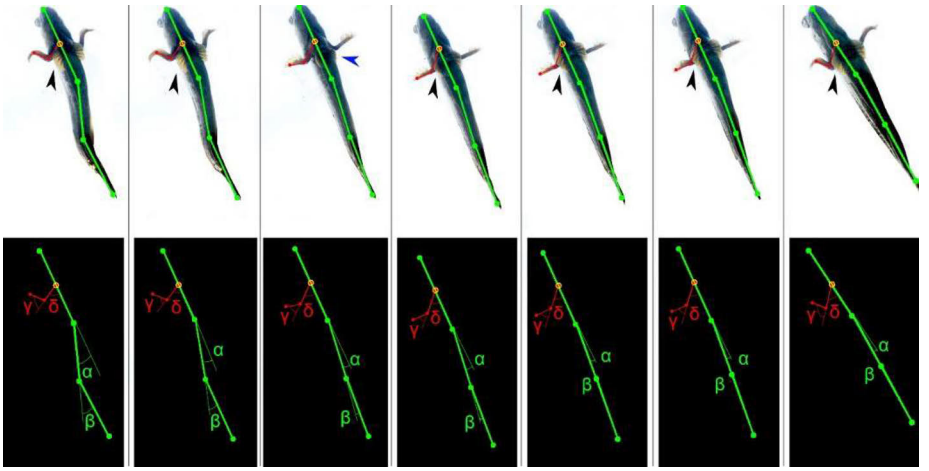

Figure 4.18. The body, pectoral fins, and pelvic fin displacement of *P. variabilis* during crutching kinematics. The black arrows on the fish images indicate the pelvic fin rays during substrate attachment; the blue arrow indicates the moment the pelvic fins are pulled from the initial position on the substrate. The angles of the cranium-midsection deflection are marked with α; those of the midsection-caudal deflection are marked with β. The angles of the pectoral fin radial-ray and radial-main body deflections are marked with γ and δ, respectively. The fish kinematics image is from Wicaksono et al. (2016; **Paper I**).

Table 4.1. The angle shift steps (1–7) during crutching kinematics (relative to the proximal segment).

Section	Symbol	Angle (°)						
		1	2	3	4	5	6	7
Midsection	α	-21	-14	-7	-12	-4	-4	-4
Caudal	β	25	16	8	7	0	0	0
Pectoral Ray	γ	-78	-75	-60	-60	-50	-54	-101
Pectoral Radial	δ	-60	-63	-50	-45	-42	-42	-46

Note: Positive angle = to the right side of the body; negative angle = to the left side of the body. The observed pectoral fin is the left part only.

From the observations made in Fig. 4.18, we obtained the deflection angles, as shown in Table 4.1. It appears that during crutching, the mid-to-caudal section does not contribute to forward locomotion. No dramatic change appears to facilitate movement, as the caudal section simply straightens itself to align with the midsection. During the crutching locomotion, the pectoral fins actively push the body by swinging backwards; this can be seen in steps 1–6, as the left pectoral fin angles γ and δ shift during. In steps 6–7, the left pectoral fin radial recovers, and the angle rapidly increases from 42° to 46° (in the left direction, hence the value is negative); the pectoral radial moves drastically forward from 54° to 101°.

To mimic the body movement in RoboAnalyzer, the mid-to-causal section is set to move in two steps: First, the midsection is set to move from -21° to -12° while the caudal section is set to move from 25° to 7° (to mimic steps 1–4 in Table 4.1). Second, the midsection is set to move from -12° to -4° while the caudal section is set to move from 7° to 0° (aligning the caudal section fully with the midsection to mimic step 5–7 in Table 4.1). Throughout the simulation, the cranial section is set to static (kept at 0°). The result is depicted in Fig. 4.19. While the cranial section stays in its position (green section), the midsection and caudal section move lightly from the initial (Fig. 4.19A) to final (Fig. 4.19B) steps, alongside the slight displacements at the end (Fig. 4.19B–D). The plots of the corresponding links end the stance changes in Fig. 4.19 at the X-Y-Z Cartesian axes, which can be seen in Fig. 4.20.

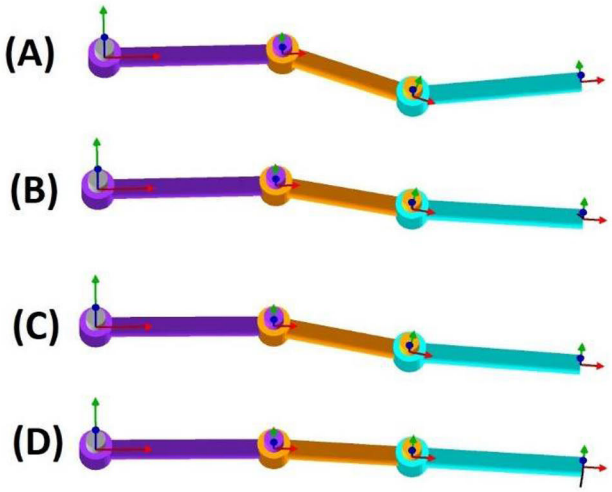

Figure 4.19. The body stances of *P. variabilis* during crutching kinematics (with few caudal body involvement, as in Fig. 4.18) as simulated in RoboAnalyzer in two phases: (A–B) initial steps (angle of cranial section-midsection: -21° to -12°; angle of midsection-caudal section: 25° to 7°) and (C–D) final steps (angle of cranial section-midsection: -12° to -4°; angle of midsection-caudal section: 7° to 0°). Purple is the cranial section, orange is the midsection, and cyan is the caudal section.

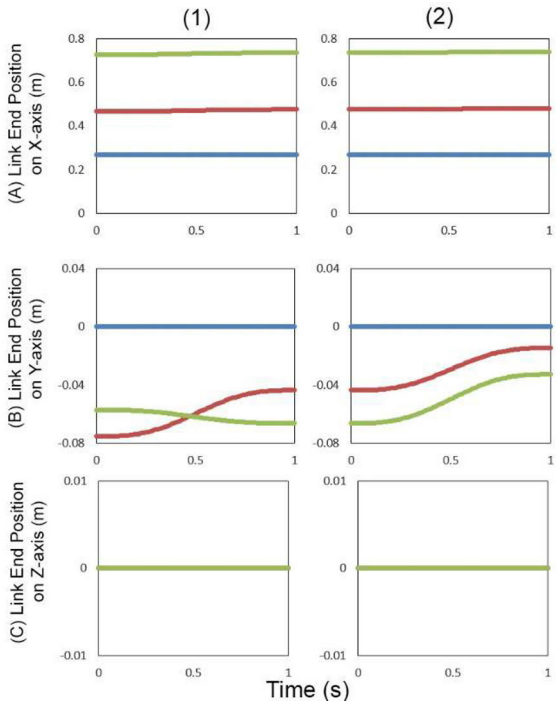

Figure 4.20. The body links end the stance changes within the Cartesian axes during the initial phase of crutching (steps A–B, as in Fig. 4.19; 1) and the final phase of crutching (steps C–D, as in Fig. 4.19; 2), showing the distance on the X-axis (A), Y-axis (B), and Z-axis (C). Colour code: Joint 1 (cranial section) – Blue; Joint 2 (midsection) – Red; Joint 3 (caudal section) – Green. Negative values indicate movement in the opposite direction.

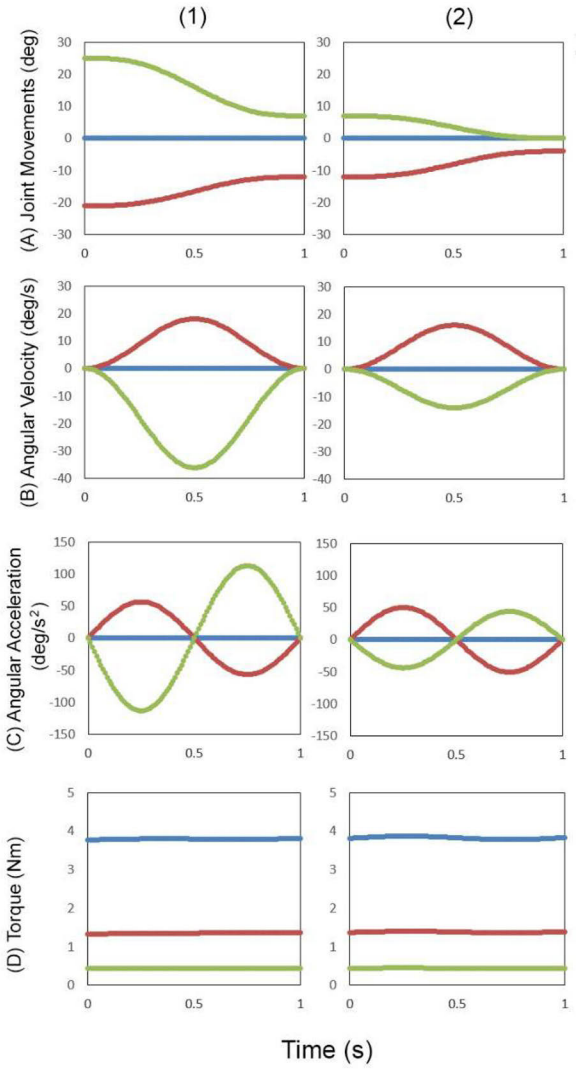

Figure 4.21. Kinetic measurements of the body-revolving joints during the initial phase of crutching (steps A–B, as in Fig. 4.19; 1) and the final phase of crutching (steps C–D, as in Fig. 4.19; 2), showing angular movement (A), angular velocity (B), angular acceleration (C), and torque (D). Colour code: Joint 1 (cranial section) – Blue; Joint 2 (midsection) – Red; Joint 3 (caudal section) – Green. Negative values indicate movement in the opposite direction.

Following the simulation, the positions of the link ends (the tips of the link) appear to only be transverse in the X and Y axes (Fig. 4.20). In the X-axis plot, all of them are relatively still, with joint 1 (blue, Fig. 4.20A) moved in the stable Y-axis of the X-plot. With the Y-axis serving as a point of comparison, joint 1 is visibly immobile, as joint 2 swings toward the higher axis and joint 3 overlaps with joint 2 (Fig. 4.20B1) before they synergistically move together in step 2 (Fig.

4.20B2). None are moving on the Z-axis, as no twist was set (Fig. 4.20C). For the joint kinetics (Fig. 4.21), joint 1 seems to stand still, as the cranial section was set to immobile, and joints 2 and 3 move toward the position of joint 1 (straight line) in steps 1 and 2 (compare Fig. 4.19 A–B and C–D to Figs. 4.21A1 and 4.21A2). The velocity of movement toward the straightening is faster during step 1 (Fig. 4.21B1) than step 2 (Fig. 4.21B2). The acceleration graphic profile is also similar (Fig. 4.21C). As joint 1 must compensate for the forces caused by the movement of the other joints, the torque in joint 1 has the highest value, followed by joint 2 (as it compensates for the force from joint 3).

To simulate the piston-like pelvic deployment during crutching, the RoboAnalyzer simulation starts from the moment at which the pelvic fins are pulled as the mudskipper move forwards (Fig. 4.18, steps 3–4; blue arrow points to where the pelvic fin ray is pulled while the black arrow points to where the pelvic fin ray touches the substrate underneath). The model sections have three DOF for the pelvic-pectoral model and are set to PRR (prismatic-revolving-revolving) mode: the first link is prismatic (piston-like) to mimic the pelvic displacement while the rest are revolving to mimic the pectoral fin. The length of the first section link is set to 0.05m to mimic a realistic pectoral radial next to the pelvic girdle, while the second (ray) is 0.08m, and both set with 1 g of weight. The result is the pelvic downward displacement (0.033m in the model) like a piston during a 5° radial (partial, instead of full) backswing (according to pectoral radial swing in Fig. 4.18, steps 3–4; Fig. 4.22A) for the pelvic-pectoral model. The second link for the pectoral model completes the backswing of the pectoral radial, as in Fig. 4.18 (step 2), where the angle is at its high point of -63°, to step 6, where the angle is at -42°. However, the ray follows the transition from steps 2 to 5 (from -75° to 50°). The result is displayed in Fig. 4.22B. After the backswing, the ray performs a wide-recovery front swing (steps 6–7; from -50° to -101°) while the radial does only a narrow front swing (from -42° to -46°) as it initiates forward movement (Fig. 4.22C).

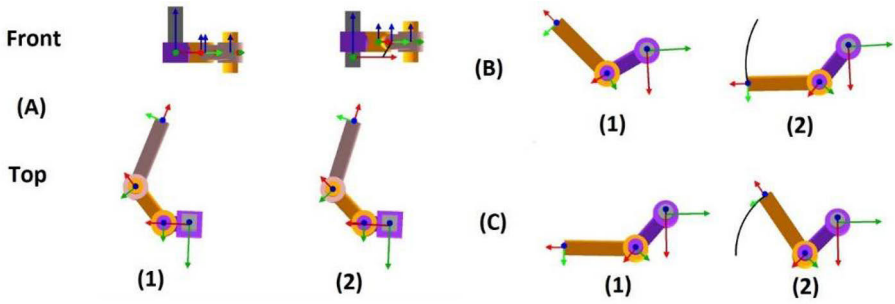

Figure 4.22. The two RoboAnalyzer models on the downward deployment of the pelvic fin girdle (0.033m) upon abduction by the pectoral fin muscle (A), the pectoral fin backswing (B), and the recovery front swing (C). The purple in A is the pectoral radial joint that connects to the pelvic girdle compound joints. The purple in B and C is the pectoral fin radial. The orange in A is the pectoral fin radial while the orange in B and C is the pectoral fin ray. The grey in A is the pectoral fin ray.

The graphics below were generated by RoboAnalyzer. The first two come from the pectoral radial-ray interaction (Figs. 4.22B and C; the graphics: Figs. 4.23 and 4.24). The second two come from the backswing of the pectoral fin and its effect on the pelvic girdle's piston-like displacement (Fig. 4.22A; the graphics: Figs. 4.25 and 4.26).

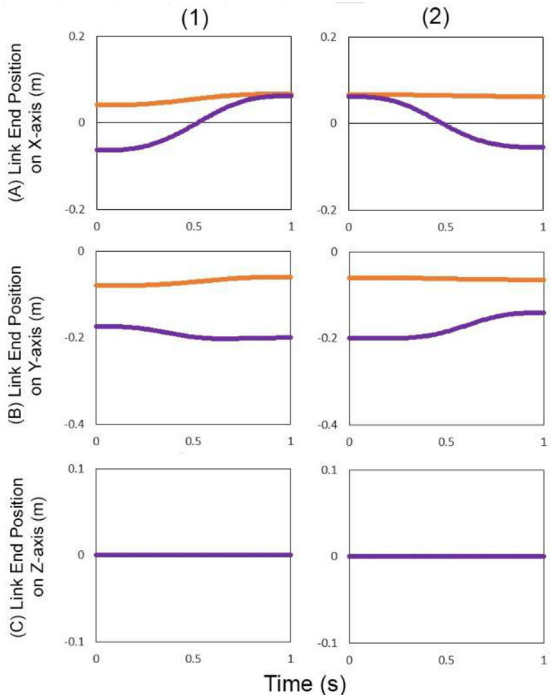

Figure 4.23. The pectoral fin link end positions at the Cartesian axes during the backswing (Fig. 4.22B; 1) and the recovery front swing (Fig. 4.22C; 2), showing the distance on the X-axis (A), Y-axis (B), and Z-axis (C). Colour code: Joint 1 (radial section) – Orange; Joint 2 (ray section) – Purple. Negative values indicate movement in the opposite direction.

The pectoral fin radial was set to move less than the ray section in both full backswing (Fig. 4.23.1) and recovery front swing (Fig. 4.23.2), as seen by the ray section moving more freely in Figs. 4.23A and B. No movement can be observed on the Z-axis, as there was no Z-axis twist. Kinetically, the ray and radial move

synchronously during the backswing (Fig. 4.24A1); in contrast, during the recovery front swing, the ray section moves in a distinct manner (Fig. 4.24A2). The ray and radial have identical velocities during the backswing (Fig. 4.24B1); however, during the recovery front swing, the ray section moves faster than the radial (Fig. 4.24B2) in the opposite direction. This synchronization could also be seen in the acceleration pattern (Fig. 4.24C). The radial torque is higher than the ray torque during both the backswing and recovery front swing, as the radial takes the swinging force of the ray section (Fig. 4.24D).

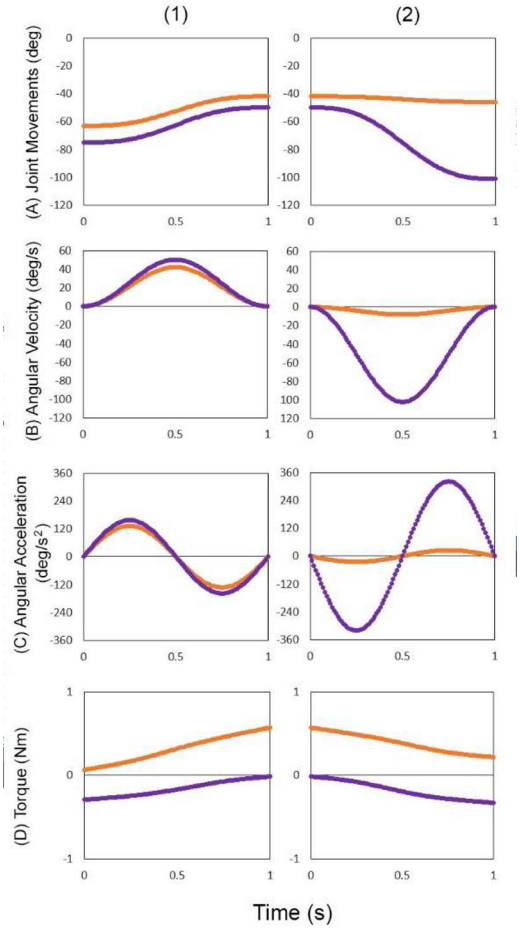

Figure 4.24. The pectoral fin joint changes during both the backswing (Fig. 4.22B; 1) and the recovery front swing (Fig. 4.22C; 2), showing the angular movement (A), angular velocity (B), angular acceleration (C), and torque (D). Colour code: Joint 1 (radial/proximal section of pectoral fin) – Orange; Joint 2 (ray/distal section of the pectoral fin) – Purple. Negative values indicate movement in the opposite direction.

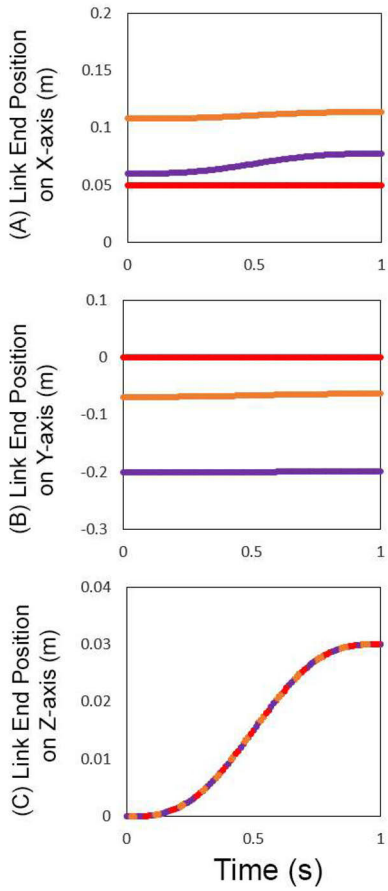

Figure 4.25. The pectoral fin-pelvic fin girdle link end is positioned within the Cartesian axes during the partial backswing with piston-like displacement of pelvic girdle (Fig. 4.22A), showing the distance on the X-axis (A), Y-axis (B), and Z-axis (C). Colour code: Joint 1 (pectoral radial joint-pelvic girdle) – Red; Joint 2 (pectoral radial section) – Orange; Joint 3 (pectoral ray section) - Purple. Negative values indicate movement in the opposite direction. In C, all move on the same Z-axis (the curve is in the augmented red-orange-purple).

During the revolving action of the pectoral fin through a partial backswing with prismatic movement in the pelvic girdle, both the pelvic girdle (Figs. 4.25A and B, red) and the pectoral radial (Figs. 4.25A and B, orange) are relatively stable. However, the pectoral ray moves slightly on the X-axis (Fig. 4.25A, purple). On the Z-axis, all move positively as the pelvic girdle-pectoral fin system displaces the piston downward while the rest of the system moves upward on the positive side of the Z-axis (Fig. 4.25C).

As only the pectoral fin radial (Fig. 4.26, orange) is moving, only the radial shows slight movement; the pectoral ray (Fig. 4.26, purple) just moves stably

(Fig. 4.26A) while the pelvic girdle shows no movement (Fig. 4.26, red). Thus, only the radial generates velocity (Fig. 4.26B) and and acceleration pattern (Fig. 4.26C). As for torque and generated force (Fig. 4.26D), the pelvic girdle (red) experiences the force generated by the piston-like movement—the sine movements represent the force during initial deployment and halt at the end of movement. The pectoral radial (orange) experiences the highest torque, as it handles the force of the pectoral ray (purple). This is similar to the other simulation, in which the axis handles the end-site of the joint.

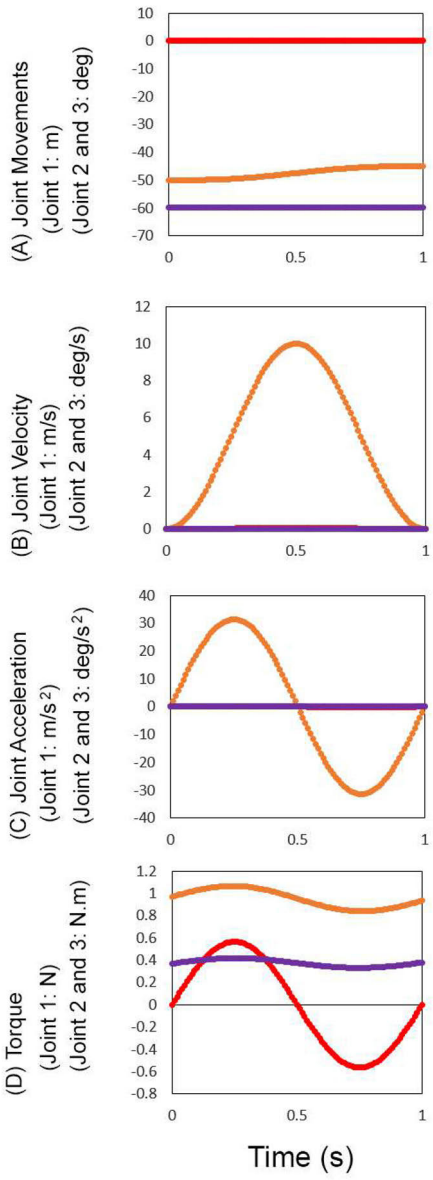

Figure 4.26. The pectoral fin-pelvic fin girdle joint changes during the partial backswing with the piston-like displacement of pelvic girdle (Fig. 4.22A), showing the angular change (A), angular velocity (B), angular acceleration (C), and torque (D). Colour code: Joint 1 (pectoral radial joint – pelvic girdle) – Red; Joint 2 (pectoral radial section) – Orange; Joint 3 (pectoral ray section) - Purple. Negative values indicate movement in the opposite direction.

The mudskipper in this observation from Kendal rarely used its caudal section during terrestrial locomotion. It occasionally employed its caudal section

if it required sideways movement or rapid locomotion for escape purposes (Fig. 4.27). The robotic MuddyBot by McInroe (2015) also exhibited this caudal restraint, only making use of the section when the walking path became steeper.

Figure 4.27. The sideways movement of *P. variabilis* at a bamboo substrate, where the caudal body section movement is involved.

Regarding land-hopping kinematics, video observations of *P. variabilis* aligned with Swanson and Gibb (2004). *P. variabilis* bent its caudal section into a J-shape to make it parallel to the main body (laterally; Fig. 4.28, 0–73ms). The mudskipper then laterally released its caudal section with the caudal fin parallel to the substrate to act as a spring, pushing the body forward and airborne as the body returns to its straight position (Fig. 4.28, 73–117ms).

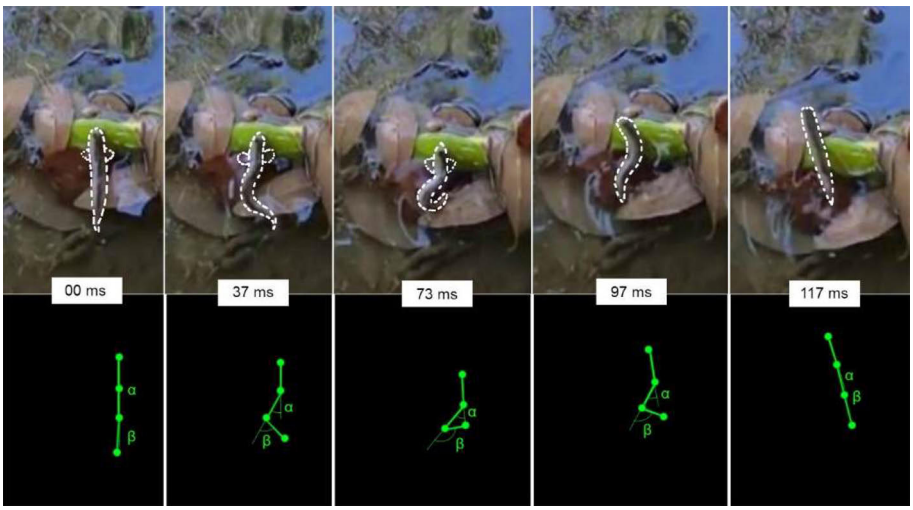

Figure 4.28. *P. variabilis* land-hopping kinematics sequence. The cranial section-midsection deflection angles are marked with α; the midsection-caudal section deflection angles are marked with β. The fish outlines are marked with continuous white dots. The fish kinematics image comes from Wicaksono et al. (2020; **Paper III**), taken with GoPro Hero 7 Black with 240 FPS.

Table 4.2. Angle shifts during land-hopping kinematics (relative to the proximal segment).

Segment	Symbol	Angle (°)

		1	2	3	4	5
Midsection	α	0	-32	-46	-40	-3
Caudal	β	-3	75	135	100	0

Note: Positive angle = to the right side of the body; negative angle = to the left side of the body.

When testing with RoboAnalyzer, the simulation was divided into two parts: the coiling, initial step, during which the caudal section forms a J-shape (Fig. 4.29, Table 4.2, step 1–3), and the release step, during which the mudskipper pushes the caudal section back to the straight position (Fig. 4.29, Table 4.2, step 3–5). As the actual structure of the robot is assumed to be sticking to the ground (no joint extrusion like in the RoboAnalyzer model), no tail twisting was added, as the hopping Z-axis trajectory (airborne trajectory) is controlled by the lifting of the pectoral fins from the ground.

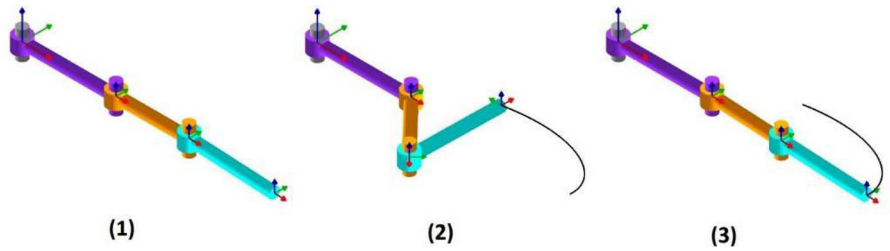

Figure 4.29. The land-hopping kinematics of *P. variabilis*, as simulated in RoboAnalyzer, showing two steps of three stances: the J-form (or initial step), during which the caudal section is folded toward the body axis (step 1–2), and the final step, during which the caudal section is released to propel the body to the air (steps 2–3). Purple is the cranial section, orange is the midsection, and cyan is the caudal section.

The positional graphics during the initial and final steps of the kinematics are symmetrical in the X, Y, and Z axes (Figs. 4.30.1 and 4.30.2). This is because, at the initial step, the mudskipper (despite small angular differences) takes the J-form (Fig. 4.29; steps 1–2; Fig. 4.30A1) and returns to the straight line at the final step (Fig. 4.29; steps 2–3; Fig. 4.30A2). The angular velocity and acceleration profiles are also symmetrical (Figs. 4.31B and C; steps 1 and 2). In this modelling, there was no acceleration during the change from the J-form to the straightening, which is supposed to be faster with the pectoral fins deployed to the ground to control the body's aerial trajectory, as shown in Swanson and Gibb (2004). However, in RoboAnalyzer, the velocity was set as uniform during the modelling. In the software, it is more challenging to twist the pectoral fin joint downward to imitate the actual pectoral fin biological joint. It can be added to the actual design of the robot in the future.

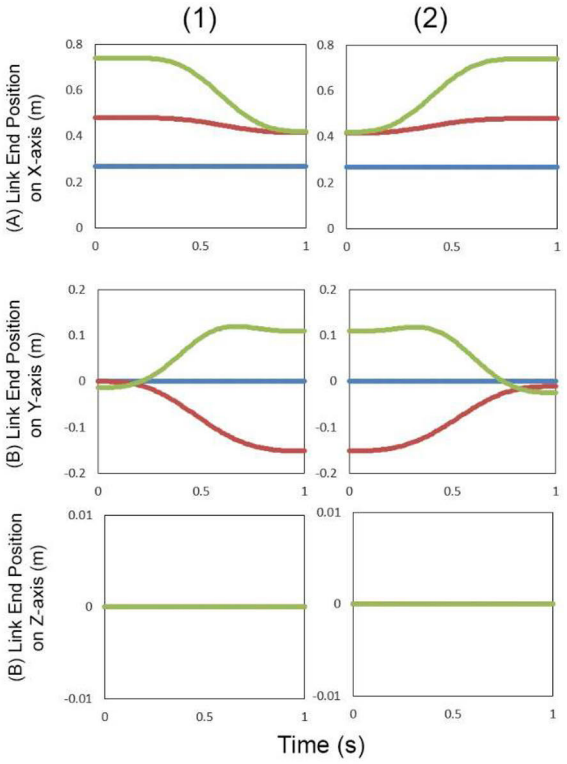

Figure 4.30. The body link end positions within the Cartesian axes during the initial step of land-hopping (steps 1–2 in Fig. 4.29; 1) and the final step of land-hopping (steps 2–3 in Fig. 4.29; 2), showing the distance on the X-axis (A), Y-axis (B), and Z-axis (C). Colour code: Joint 1 (cranial section) – Blue; Joint 2 (midsection) – Red; Joint 3 (caudal section) – Green. Negative values indicate movement in the opposite direction.

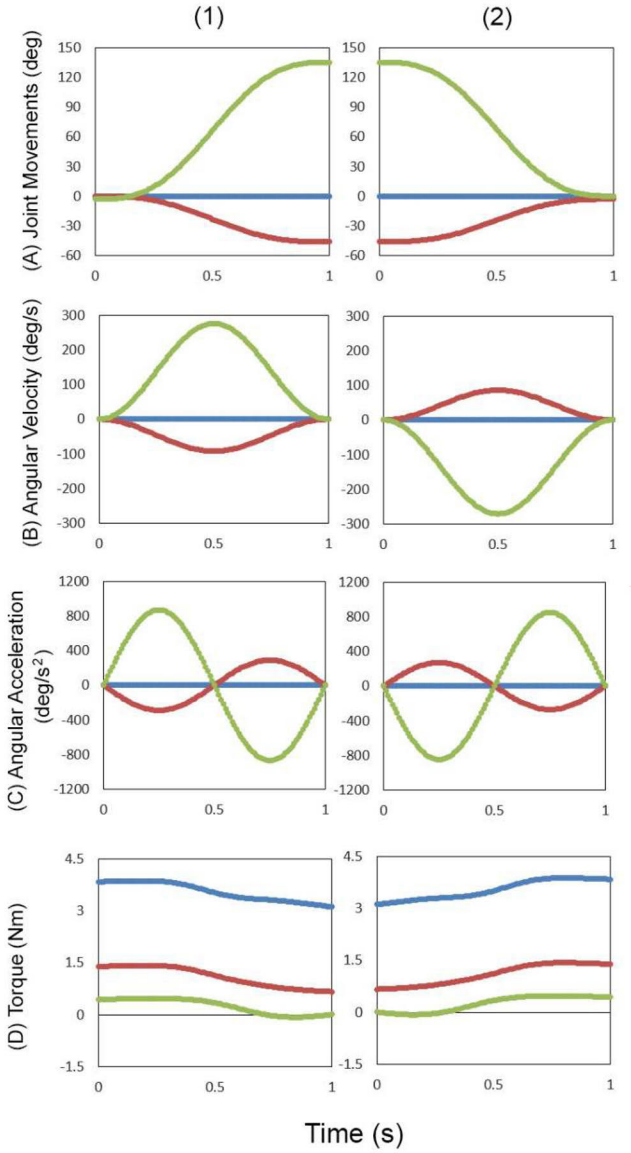

Figure 4.31. The body joint changes during the initial step of land-hopping (steps 1–2 in Fig. 4.29; 1) and the final step of land-hopping (steps 2–3 in Fig. 4.29; 2), showing the angular movement (A), angular velocity (B), angular acceleration (C), and torque (D). Colour code: Joint 1 (cranial section) – Blue; Joint 2 (midsection) – Red; Joint 3 (caudal section) – Green. Negative values indicate movement in the opposite direction.

During the modelling, as with the rest of the kinematics, the cranial section was immobile, the midsection moved relatively freely, and the caudal section took on a J-form and displayed greater movement (Fig. 4.31A1, initial state; Fig.

4.31A2, final state). As the caudal (green) is also involved in the J-form, the velocity and acceleration (Fig. 4.31B and C) of the caudal section (green) also peaked at the midsection (red; note the cranium; blue; which did not move). The torque experienced in the cranial section (blue) is the highest, as with crutching, followed by the midsection (red), and the caudal section (green); this is because the cranial section, despite being immobile, suspends the forces of the other joints and links as they move (Fig. 4.31D).

The movements are rather simple for water-hopping. The most important aspect to assess is the taxiing, as any observed airborne movements presumably do not contribute to a change in trajectory. In Fig. 4.32 and Table 4.3, the angular deflection of the caudal section of the body is similar, at 18° (despite being initiated at 25°), in each lateral direction; in the initial airborne step, the deflection stops (Fig. 4.32, airborne stage; Table 5A1 and A2). Hence, the simulation is focused on modelling the taxiing stage.

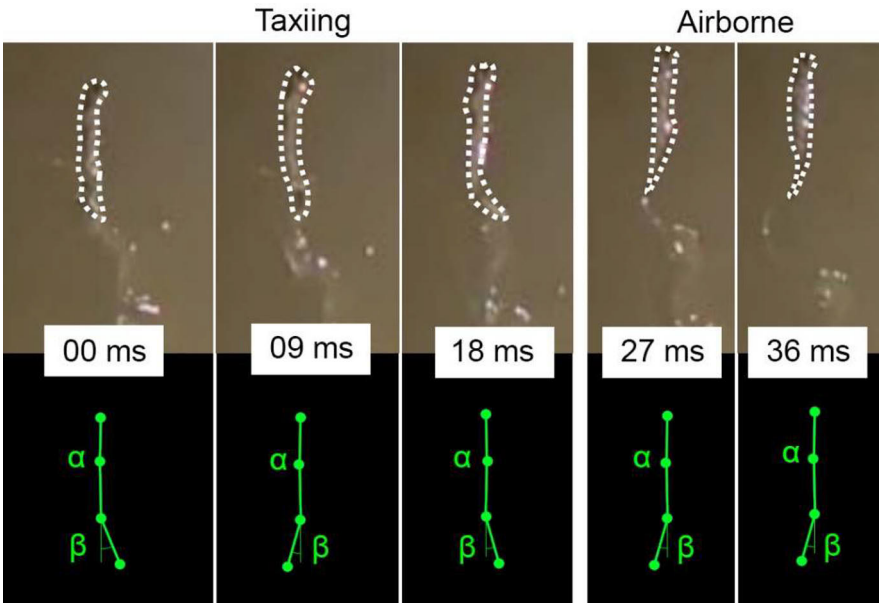

Figure 4.32. *P. variabilis* water-hopping with taxiing and airborne kinematics. The angles of the body cranium-midsection deflection are marked with α; those of the midsection-caudal section deflection are marked with β. The fish outlines are marked with continuous white dots. The fish kinematics image comes from Wicaksono et al. (2020; **Paper III**), and the picture is modified from Figure 4 in the article, taken with GoPro Hero 7 Black with 240 FPS.

Table 4.3. Angle shifts during water-hopping (taxiing [T], and airborne [A]) kinematics (relative to the proximal segment).

Segment	Symbol	Angle (°)				
		T1	T2	T3	A1	A2
Midsection	α	0	0	0	0	0
Caudal	β	-25	18	-18	18	18

Note: Positive angle = to the right side of the body; negative angle = to the left side of the body.

Using RoboAnalyzer, only the caudal section (joint 3) was set to move during the taxiing simulation. The result of cyclic lateral movement can be seen in Fig. 4.33, depicting the caudal section of the body being swung from one direction to another.

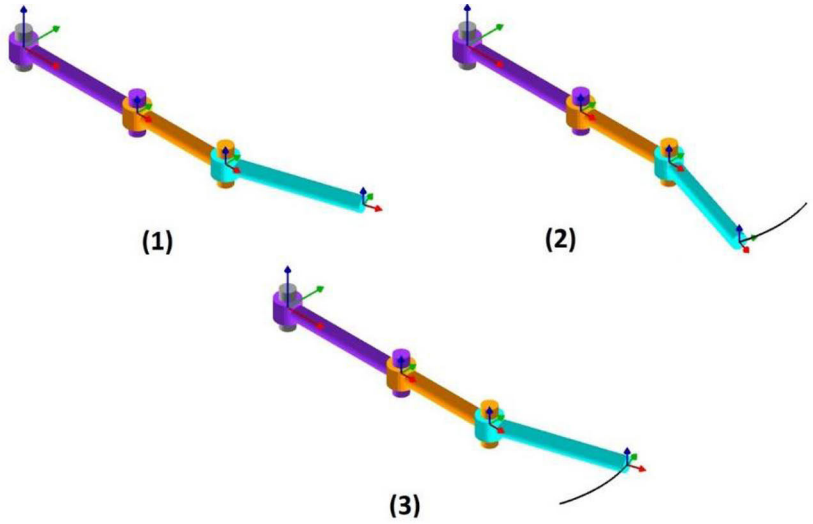

Figure 4.33. *P. variabilis* taxiing (from water) kinematics, as simulated in RoboAnalyzer, showing the cyclic caudal movement between -18° and 18° (steps 1–2 [step 1 in Fig, 4.32] and 2–3 [step 2 in Fig. 4.32], respectively). Purple is the cranial section, orange is the midsection, and cyan is the caudal section.

Similar to the land-hopping J-form stance (Fig. 4.28), the resulting link end graphic is symmetrical (Fig. 4.34). However, instead of involving the midsection for the kinematics, only the caudal section is allowed to move; this can be seen in Fig. 4.34B, where the caudal section (green) moves on the Y-axis.

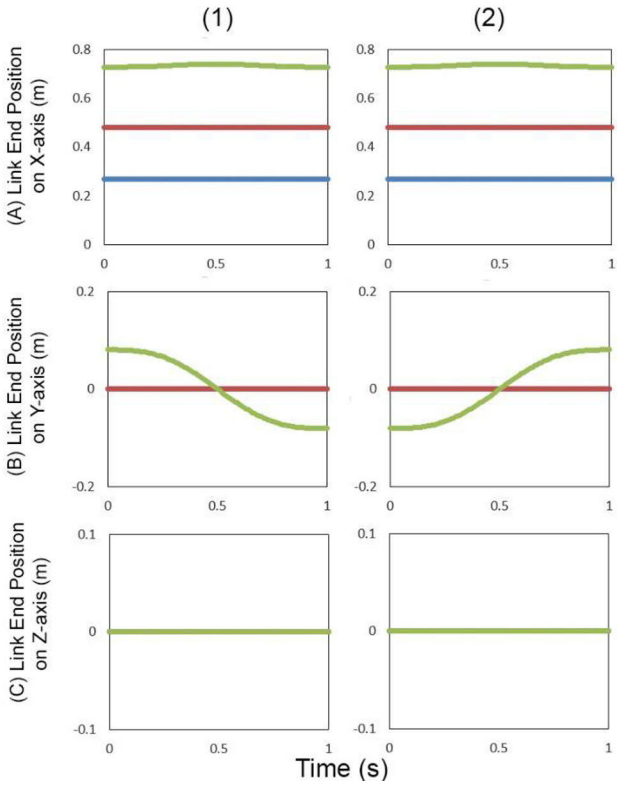

Figure 4.34. The body link end disposition within the Cartesian axes during taxiing kinematics (steps 1–2 of Fig. 4.33 in 1; steps 2–3 of Fig. 4.33 in 2), showing the distance on the X-axis (A), Y-axis (B), and Z-axis (C). Colour code: Joint 1 (cranial section) – Blue; Joint 2 (midsection) – Red; Joint 3 (caudal section) – Green. Negative values indicate movement in the opposite direction.

As the angular deflection of the caudal section (green) is only 18° from one side to another, the resulting graphics of the joints' angular movements, increase in velocities, and acceleration-deceleration patterns are also symmetrical and consistent, as the movements are cyclical (Figs. 4.35A–C). Additionally, the torque is similar to the rest of the graphics of the body joints in land hopping and crutching—highest at the cranial section, lowest at the caudal section (Fig. 4.35D).

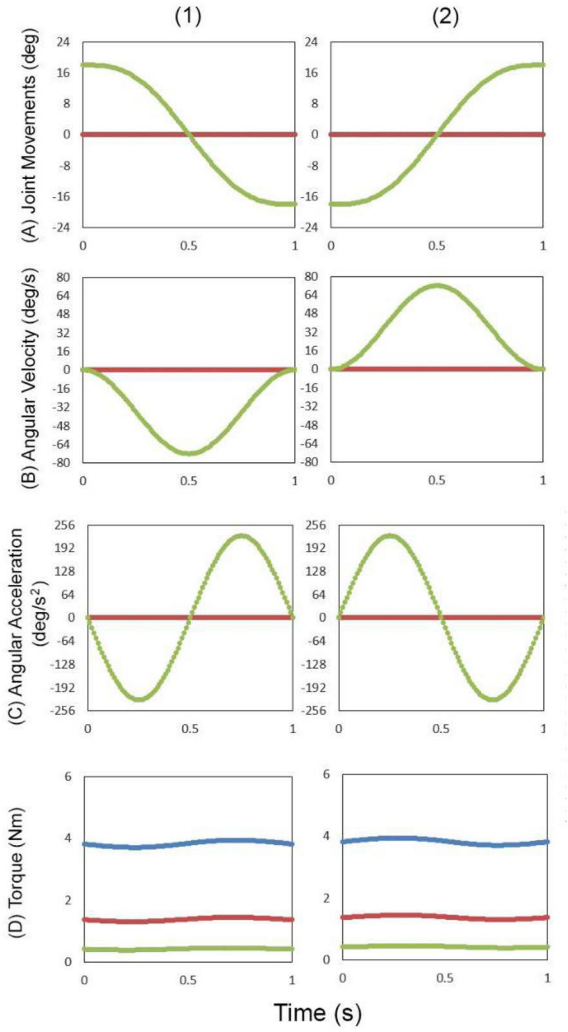

Figure 4.35. The body joint changes during taxiing kinematics (steps 1–2 of Fig. 4.33 in 1; steps 2–3 of Fig. 4.33 in 2), showing the angular movement (A), angular velocity (B), angular acceleration (C), and torque (D). Colour code: Joint 1 (cranial section) – Blue; Joint 2 (midsection) – Red; Joint 3 (caudal section) – Green. Negative values indicate movement in the opposite direction.

Following the action of forward kinematics, through which the initial and final angles are set to each kinematics movement, the final positions of the joints and links can be acquired; thus, the link end positions with the angular displacement/movements, velocity, and acceleration can also be determined. Once the angular movement (r) is available (Eq. 4.4), the angular velocity (ω) can technically be determined, as velocity is basically the derivative of the movement function with time (Eq. 4.5). Similarly, angular acceleration (α) constitutes a derivative of the velocity function with time (Eq. 4.6).

$$r(t) = x \tag{4.4}$$

$$\omega(t) = \frac{d}{dt} r(t) = \frac{d}{dt} x = xt^{-1} \tag{4.5}$$

$$\alpha(t) = \frac{d}{dt} \omega(t) = \frac{d}{dt} xt^{-1} = xt^{-2} \tag{4.6}$$

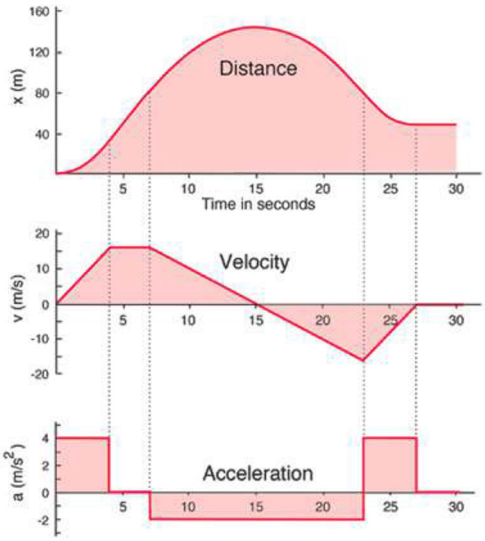

Figure 4.36. The general simplified graphic of relations between movement distance, velocity, and acceleration (source: hyperphysics.phy-astr.gsu.edu).

The robot model movements are following the graphics (Fig. 4.36), the velocity increases at the early stage alongside the increase in movement distance. It then becomes more stationary as movement distance rises in a more stable manner (almost linearly). Once movement peaks, velocity drops to stop position, instead of stopping suddenly. The same condition applies when the body moves in the opposite direction, where the velocity is negative. Acceleration rises when velocity increases and drops when velocity decreases. When velocity is stable, acceleration is near zero.

During the simulation, the force given to each of the links is assumed to be uniform. However, in the RoboAnalyzer (according to Prof. Dr. Subir Kumar Saha, the developer of RoboAnalyzer; pers. comm.), the immobile cranial section, or joint 1 (with angular displacement equaling zero at all times), is exposed to the greatest accumulated force, as it handles the force loaded to all links and joints (midsection and caudal section [or joints 2 and 3], with links 1, 2, and 3). Subsequently, the midsection or joint 2 handles the force loaded to its link length plus the caudal section link and joint (links 2 and 3 and joint 3). The caudal

section (joint 3) handles only its own link (link 3); hence, it constantly has the lowest torque. The force experienced by joint 1 (cranial) is analogous to how our shoulder handles the force when our upper arm is static but our lower arm and palm are moving (Fig. 4.37). This implies that the mudskipper must actively control the accumulation of force in the cranial section; hence, the cranial section must constantly redirect its position to maintain a straight trajectory (e.g., air trajectory during hopping, terrestrial trajectory during crutching, aquatic trajectory during swimming). Additionally, the body must balance the lateral force during swimming to drive forward movement (Sfakiotakis et al. 1999).

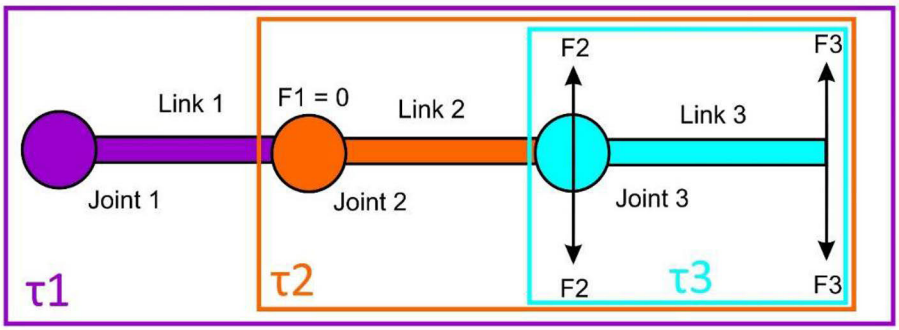

Figure 4.37. Torque (τ) measurement on each joint, with joint 1 (cranial section) experiencing τ_1, joint 2 (midsection) experiencing τ_2, and joint 3 (caudal section) experienced τ_3.

The mudskipper robot model in this study suggests some improvements to the MuddyBot's future design (McInroe 2015; Fig. 4.38):

1. Instead of being exclusively terrestrial, the new mudskipper robot could also become aquatic, supporting water-hopping or even swimming to allow the robot to move from one spot on the water surface to another.
2. By adding more DOF to the core body and pectoral fins, the robot could be more flexible to support enhanced crutching kinematics. It could even able to hop by employing the J-form on the joint between midsection-caudal sections with the body tilt to set aerial trajectory provided by the pectoral fins.
3. The caudal fin could be heterocercal, with its lower lobe wider than its upper lobe (Pough 2005). This change would add an upper lobe to the original design to provide more foil surface during swimming and taxiing.
4. Pectoral fins could be lowered and pulled off the ground to enhance grip during the crutching swing movements.
5. To bring the function close to the actual mudskipper, the robot could be lightweight, and the pelvic fins could be made from elastic material to support Stefan adhesion. Alternatively, ventral adhesion could be

provided by MRF to alter the viscosity using magnetic fields, as in the robot design of Wiltsie et al. (2012) (Fig. 4.17).

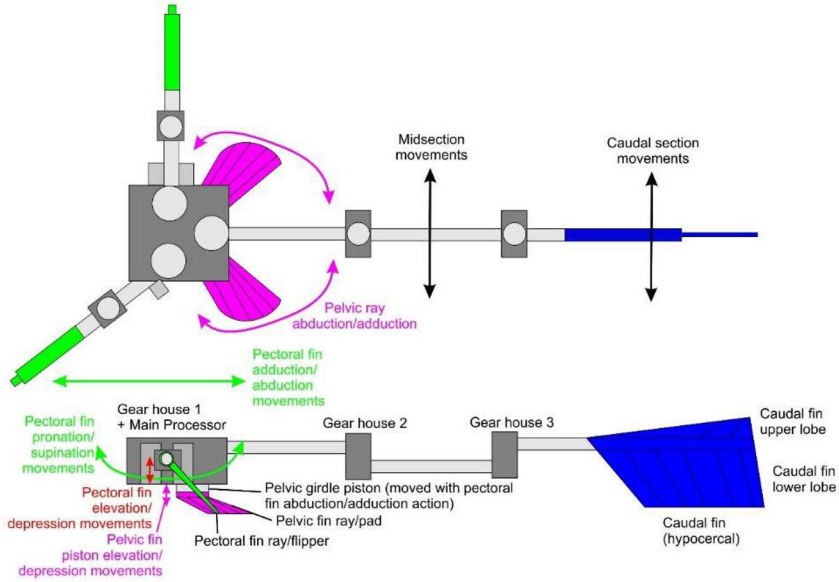

Figure 4.38. Hypothetical design improvement for improvements to the mudskipper robot (MuddyBot) to support terrestrial locomotion (crutching), land-hopping, swimming, and water-hopping. The pectoral fin axis (radial) is able to elevate and depress to enhance its grip on the substrate while retaining its abduction-adduction movements, the pectoral fin ray pronation, and supination (similar to McInroe, 2015). It features a deployable pelvic fin pad and a hypocercal caudal fin instead of a homocercal caudal fin to support the terrestrial application. The lower lobe provides grip during crutching, land-hopping, and water-hopping while the small portion of the upper lobe provide additional function as foil during swimming, when the pelvic fin ray can be adducted to the core body to reduce hydrodynamic drag.

The creation of an amphibious robot capable of swimming, hopping, and moving on land is applicable to many industries, including maintenance and military applications. It would also enhance our understanding of the precise way in which the mudskipper evolved to move on land.

5. Conclusion and Future Prospects

The mudskippers considered in this study (*P. variabilis*, *P. gracilis*, and *B. boddarti*) are fine examples of aquatic-terrestrial adaptation among modern fish. However, *B. boddarti* is more geared toward an aquatic lifestyle. Unlike *B. boddarti*, which has fused pelvic fins with low flexibility, *P. variabilis* has unfused pelvic fins with high flexibility to provide better contact with the solid substrate surface and facilitate Stefan adhesion. This enables the *P. variabilis* to stick to high-incline vertical substrates, even when its pectoral fins are fully retracted.

Terrestrial mudskippers (*P. variabilis* and *P. gracilis*) possess body morphology that enables adaptation to terrestrial locomotion to a greater degree than other fishes (in this study, the ornate goby, *I. ornatus*, is used as a point of comparison). Their pair of pectoral fin radials are located slightly ventrally to provide piston-like movement on its pelvic fins, enabling them to stabilise the body during the pectoral fins' backward stroke. The combined movement of the paired pectoral and pelvic fins is comparable to that of front limbs and hind limbs among land-based tetrapods.

Other than its fascinating terrestrial locomotion, the mudskipper (*P. variabilis*) is able to use water-hopping as an escape mechanism. This relies on cyclic, rapid lateral movements of the caudal body section to taxi and gather kinetic energy before propelling itself airborne. Their taxiing kinematics are comparable to those of the flying fish but at a far shorter distance. Upon landing, the mudskipper can redo the taxiing sequence to become airborne again; alternatively, using its remaining kinetic energy, it can bounce like a skipping rock into the air. The water-hopping can occur in a straight line, on a curve, or even in a sharp U-turn. The mudskipper could land on a solid substrate or, if it has exhausted its energy, swim using its carangiform mode of BCF swimming.

Learning from the unusual but fascinating characteristics of this terrestrial fish, it is clear that many things can be drawn from the mudskipper's design. Biomimetic designs for various applications can be build, such as controllable adhesive sheeting, bulletproof armour, robots with controllable adhesive appendages, and even mudskipper robots as forms of bionic engineering.

There are still many mudskipper species across the ten genera that have yet to be examined. Research into these remaining species would unlock other aquatic and terrestrial features from their physiology, morphology, and biomechanics. The resultant data could be developed into computer models and used for unique and fascinating design improvements.

References

Abdulghany AR (2017). Generalization of parallel axis theorem for rotational inertia. *American Journal of Physics* 85: 791-795.

Alam P (2004). *The reinforcement of timber for structural applications and repair*. Doctoral dissertation, University of Bath, United Kingdom. pp. 37-56.

Alkrad JA, Mrestani Y, Stroehl D, Wartewig S, Neubert R (2003). Characterization of enzymatically digested hyaluronic acid using NMR, Raman, IR, and UV–Vis spectroscopies. *Journal of Pharmaceutical and Biomedical Analysis* 31: 545-550.

Bahuguna J, Chittawadigi RG, Saha SK (2013). Teaching and learning of robot kinematics using RoboAnalyzer software. In: *Proceedings of Conference on Advances In Robotics* (pp. 1-6).

Balaban JP, Summers AP, Wilga CA (2015). Mechanical properities of the hyomandibula in four shark species. *Journal of Experimental Zoology* 323: 1–9.

Band YB, Avishai Y (2013). 3-Angular Momentum and Spherical Symmetry. In: *Quantum Mechanics with Applications to Nanotechnology and Information Science*, pp.105-157.

Britz R, Johnson GD (2012). Ontogeny and homology of the skeletal elements that form the sucking disc of remoras (Teleostei, Echeneoidei, Echeneidae). *Journal of Morphology* 273: 1353-1366.

Budi AS, Widiyani T, Budiharjo A (2018) Daily behavior of the mudskippers at Wonorejo Mangrove Forest Surabaya. In: *AIP Conference Proceedings* (Vol. 2002, No. 1, p. 020003). AIP Publishing LLC.

Budney LA, Hall BK (2010). Comparative morphology and osteology of pelvic fin-derived midline suckers in lumpfishes, snailfishes and gobies. *Journal of Applied Ichthyology* 26: 167-175.

Buttkus H (1963). Red and white muscle of fish in relation to rigor mortis. *Journal of the Fisheries Research Board Canada* 20: 45–58.

Case DA, Cheatham TE, Darden T, Gohlke H, Luo R, Merz KM, Onufriev A, Simmerling C, Wang B, Woods RJ (2005). The amber biomolecular simulation programs. *Journal of Computational Chemistry* 26,:1668–1688.

Courant R (1943). *Variational methods for the solution of problems of equilibrium and vibrations*. Verlag nicht ermittelbar.

Davenport J, Matin AA (1990). Terrestrial locomotion in the climbing perch, *Anabas testudineus* (Bloch) (Anabantidea, Pisces). *Journal of Fish Biology* 37: 175-184.

Davenport J (1994). How and why do flying fish fly? *Reviews in Fish Biology and Fisheries* 4: 184-214.

de Hoog HPM, Arends IW, Rowan AE, Cornelissen JJ, Nolte RJ (2010). A hydrogel-based enzyme-loaded polymersome reactor. *Nanoscale* 2: 709-716.

Denavit J, Hartenberg RS (1955). A kinematic notation for lower-pair mechanisms based on matrices. *Journal of Applied Mechanics, Transactions ASME* 215–221.

Dirks J-H (2014). Physical principles of fluid-mediated insect attachment – Shouldn't insect slip? *Beilstein Journal of Nanotechnology* 5: 1160-1166.

Domel AG, Saadat M, Weaver JC, Haj-Hariri H, Bertoldi K, Lauder GV (2018). Shark skin-inspired designs that improve aerodynamic performance. *Journal of the Royal Society Interface*, *15*(139), p.20170828.

Don EK, Currie PD, Cole NJ (2013). The evolutionary history of the development of the pelvic fin/hindlimb. *Journal of Anatomy* 222: 114-133.

Esmaeili HR, Hojat AT, Teymouri A (2007). Scale structure of a cyprinid fish, *Capoeta damascina* (Valenciennes in Cuvier and Valenciennes, 1842) using scanning electron microscope (SEM). *Iranian Journal of Science & Technology* 31.

Ewoldt RH, Tourkine P, McKinley GH, Hosoi AE (2011). Controllable adhesion using field-activated fluids. *Physics of Fluids* 23: 073104.

Farhat W, Venditti RA, Hubbe M, Taha M, Becquart F, Ayoub A (2016). A review of water-resistant hemicellulose-based materials: processing and applications. *ChemSusChem* 10: 305-323.

Fish FE (1990). Wing design and scaling of flying fish with regard to flight performance. *Journal of Zoology* 221: 391-403.

Flammang BE, Suvarnaraksha A, Markiewicz J, Soares D (2016). Tetrapod-like pelvic girdle in a walking cavefish. *Scientific Reports* 6: 1-8.

Fricke H, Hissmann K (1992). Locomotion, fin coordination and body form of the living coelacanth *Latimeria chalumnae*. *Environmental Biology of fishes* 34: 329-356.

Garrano AMC, la Rosa G, Zhang D, Niu LN, Tay FR, Majd H, Arola D (2012). On the mechanical behavior of scales from *Cyprinus carpio*. *Journal of the Mechanical Behavior of Biomedical Materials* 7: 17-29.

Genten F, Terwinghe E, Danguy A (2009) *Atlas of Fish Histology*. Science Publisher, Enfield, USA.

Gibson RN (1986). Intertidal teleosts: life in a fluctuating environment. In: *The behaviour of teleost fishes* (pp. 388-408). Springer, Boston, MA.

Gibson AP, Riley J, Schweiger M, Hebden JC, Arridge SR, Delpy DT (2003). A method for generating patient-specific finite element meshes for head modelling. *Physics in Medicine & Biology* 48: 481.

Grant JA, Pickup BT, Sykes MJ, Kitchen CA, Nicholls A (2007). A simpleformula for dielectric polarisation energies: the Sheffield Solvation Model. *Chemistry and Physics Lett*er 441: 163–166.

Gupta V, Chittawadigi RG, Saha SK (2017). RoboAnalyzer: robot visualization software for robot technicians. In: Proceedings of the Advances in Robotics (June 2017). 26: 1-5.

Harris VA (1960). April. On the locomotion of the mud-skipper *Periophthalmus koelreuteri* (Pallas): (Gobiidae). In: *Proceedings of the Zoological Society of London* (Vol. 134, No. 1, pp. 107-135). Blackwell Publishing Ltd, Oxford, UK.

Hidayat S (2015). Struktur histologi dan morfokinetik sirip perut ikan gelodok *Periophthalmus variabilis* (Eggert, 1935) dan *Boleopthalmus boddarti* (Pallas, 1770). Master Thesis, Universitas Gadjah Mada, Indonesia.

Hidayat S, Wicaksono A, Raharjeng A, Jin DSM, Alam P, Retnoaji B (2022) The morphologies of mudskipper pelvic fins in relation to terrestrial and climbing behaviour. *Proceedings of Zoological Society* (in press).

Holmgren A (2008). *Biochemical control aspects in lignin polymerization*. Doctoral dissertation, KTH, Sweden. p. 3

Hsieh STT (2010). A locomotor innovation enables water-land transition in a marine fish. PloS One 5: e11197.

Johnston BP, Sullivan Jr, JM, Kwasnik A (1991). Automatic conversion of triangular finite element meshes to quadrilateral elements. *International Journal for Numerical Methods in Engineering* 31: 67-84.

Kawano SM, Blob RW (2013). Propulsive forces of mudskipper fins and salamander limbs during terrestrial locomotion: implications for the invasion of land. *Integrative and Comparative Biology* 53: 283-294.

Khazraji AC, Robert S (2013). Interaction effects between cellulose and water in nanocrystalline and amorphous regions: A novel approach using molecular modeling. *Journal of Nanomaterials* 2013.

King DR., Sun TL, Huang Y, Kurokawa T, Nonoyama T, Crosby AJ, Gong JP (2015). Extremely tough composites from fabric reinforced polyampholyte hydrogels. *Materials Horizons* 2: 584-591.

Kutschera U, Elliott JM (2013). Do mudskippers and lungfishes elucidate the early evolution of four-limbed vertebrates? *Evolution: Education and Outreach* 6: 1-8.

Kuusipalo J (2008). *Paper and Paperboard Converting*. Finnish Paper Engineers' Association, Helsinki, Finland. p.234.

Laurin M, Meunier FJ, Germain D, Lemoine M (2007). A microanatomical and histological study of the paired fin skeleton of the

Devonian sarcopterygian *Eusthenopteron foordi*. *Journal of Paleontology* 81: 143-153.

Lauritzen DV, Hertel F, Gordon MS (2005). A kinematic examination of wild sockeye salmon jumping up natural waterfalls. *Journal of Fish Biology* 67: 1010-1020.

Lauritzen DV, Hertel FS, Jordan LK, Gordon MS (2010). Salmon jumping: behavior, kinematics and optimal conditions, with possible implications for fish passageway design. *Bioinspiration & Biomimetics* 5: 035006.

Low WP, Lane DJW, Ip YK (1988). A comparative study of terrestrial adaptations of the gills in three mudskippers: *Periophthalmus chrysospilos*, *Boleophthalmus boddarti*, and *Periophthalmodon schlosseri*. *Biological Bulletin*, pp.434-438.

McInroe B (2015). Biological and robotic modeling of the evolution of legged locomotion on land. Undergraduate Thesis, Georgia Institute of Technology.

Murdy EO (1989). *A taxonomic revision and cladistic analysis of the oxudercine gobies (Gobiidae: Oxudercinae)*. Australian Museum, Australia.

Nesvadba P (2002) Quality control by instrumental texture measurements. In: Alasalvar C, Taylor T (eds) *Seafoods: quality technology, and neutraceutical applications*. Springer-Verlag, Berlin, pp. 48–49.

Othayoth RS, Chittawadigi RG, Joshi RP, Saha SK (2017). Robot kinematics made easy using RoboAnalyzer software. *Computer Applications in Engineering Education* 25: 669-680.

Oujebbour FZ (2014). *Methods and industrial applications in multicriteria optimization of process parameters in sheet metal forming*. Doctoral thesis, L'universite de Nice-Sophia Antipolis, France.

Pace CM, Gibb AC (2009). Mudskipper pectoral fin kinematics in aquatic and terrestrial environments. *Journal of Experimental Biology* 212: 2279-2286.

Pace CM, Gibb AC (2014). Sustained periodic terrestrial locomotion in air-breathing fishes. *Journal of Fish Biology* 84: 639-660.

Park JY (2002) Structure of the skin of an air-breathing mudskipper, *Periophthalmus magnuspinnatus*. *Journal of Fish Biology* 60: 1543-1550.

Park H, Choi H (2010). Aerodynamic characteristics of flying fish in gliding flight. *Journal of Experimental Biology* 213: 3269-3279.

Piper R (2007). *Extraordinary animals: An encyclopedia of curious and unusual animals*. Greenwood Publishing Group, Connecticut, USA, pp.250.

Polgar G (2010). Mudskippers: An Introduction For Aquarists. *Conscientious Aquarist Magazine*. http://www.wetwebmedia.com/ca/volume_7/volume_7_1/mudskippers.html [Last accessed: February 14, 2021]

Pough EH, Janis CM, Heiser JB (2005). *Vertebrate Life (7th ed)*. Pearson Education, Inc., New Jersey, USA.

Rajeevlochana CG, Saha SK (2011). RoboAnalyzer: 3D model based robotic learning software. In: International Conference on Multi Body Dynamics, pp. 3-13.

Rappé AK, Casewit CJ (1997). *Molecular mechanics across chemistry*. University Science Books, Virginia, USA. pp. 33-38

Read DA, Hover FS, Triantafyllou MS (2003). Forces on oscillating foils for propulsion and maneuvering. *Journal of Fluids and Structures* 17: 163-183.

Reuss A (1929). Berechnung der Fliessgrenz von Mischkristallen auf Grund der Plastizitatsbedingung fur Einkristalle. *Zeitschrift fur Angewandte Mathematik* 9: 49–58. (In German)

Ruiz-Torres R, Curet OM, Lauder GV, MacIver MA (2013). Kinematics of the ribbon fin in hovering and swimming of the electric ghost knifefish. *Journal of Experimental Biology* 216: 823-834.

Sayer MD (2005). Adaptations of amphibious fish for surviving life out of water. *Fish and Fisheries* 6: 186-211.

Standen EM, Du TY, Laroche P, Larsson HC (2016). Locomotor flexibility of *Polypterus senegalus* across various aquatic and terrestrial substrates. *Zoology* 119: 447-454.

Sfakiotakis M, Lane DM, Davies JBC (1999). Review of fish swimming modes for aquatic locomotion. *IEEE Journal of Oceanic Engineering* 24: 237-252.

Standen EM (2010). Muscle activity and hydrodynamic function of pelvic fins in trout (*Oncorhynchus mykiss*). *Journal of Experimental Biology* 213: 831–841.

Swanson BO, Gibb AC (2004). Kinematics of aquatic and terrestrial escape responses in mudskippers. *Journal of Experimental Biology* 207: 4037-4044.

Swennen C, Ruttanadakul N, Haver M, Piummongkol S, Prasertsongscum S, Intanai I, Chaipakdi W, Yeesin P, Horpet P, Detsathit S (1995). The five sympatric mudskippers (Teleostei: Gobioidea) of Pattani area, southern Thailand. *Natural History Bulletin of Siamese Society* 42: 109-129.

Tamura SO, Morii H, Yuzuriha M (1976). Respiration of the amphibious fishes *Periophthalmus cantonensis* and *Boleophthalmus chinensis* in water and on land. *Journal of Experimental Biology* 65: 97-107.

Thomson TJ (2019). Three-legged locomotion and the constraints on limb number: Why tripeds don't have a leg to stand on. *BioEssays* 41: 1900061.

Tran LX, Maekawa Y, Soyano K, Ishimatsu A (2020). Morphology of the feeding apparatus in the herbivorous mudskipper, *Boleophthalmus pectinirostris* (Linnaeus, 1758). *Zoomorphology* 139: 231-243.

Triantafyllou MS, Triantafyllou GS, Gopalkrishnan R (1991). Wake mechanics for thrust generation in oscillating foils. *Physics of Fluids A: Fluid Dynamics* 3: 2835-2837.

Triantafyllou GS, Triantafyllou MS (1993). Reverse Kármán Streets in the Wake of Flapping Foils for Application in Fish Propulsion. In: *Bluff-Body Wakes, Dynamics and Instabilities*. Springer, Berlin, Heidelberg, pp. 11-14.

Triantafyllou GS, Triantafyllou MS, Grosenbaugh MA (1993). Optimal thrust development in oscillating foils with application to fish propulsion. *Journal of Fluids and Structures* 7: 205-224.

Vincent JF, Bogatyreva OA, Bogatyrev NR, Bowyer A, Pahl AK (2006). Biomimetics: Its practice and theory. *Journal of the Royal Society Interface* 3: 471-482.

Wicaksono A, Hidayat S, Damayanti Y, Jin DSM, Sintya E, Retnoaji B, Alam P (2016). The significance of pelvic fin flexibility for tree climbing fish. *Zoology* 119: 511-517.

Wicaksono A, Hidayat S, Retnoaji B, Rivero-Müller A, Alam P (2017). A mechanical piston action may assist pelvic–pectoral fin antagonism in tree-climbing fish. *Journal of the Marine Biological Association of the United Kingdom*, pp.1-11.

Wicaksono A, Hidayat S, Retnoaji B, Alam P (2020). The water-hopping kinematics of the tree-climbing fish, *Periophthalmus variabilis*. *Zoology* 139: 125750.

Wiltsie N, Lanzetta M, Iagnemma K (2012). A controllably adhesive climbing robot using magnetorheological fluid. In: 2012 *IEEE International Conference on Technologies for Practical Robot Applications (TePRA)*, pp. 91-96.

Yang L, Tan C-H, Hsieh M-J, Wang J, Duan Y, Cieplak P, Caldwell J, Kollman PA, Luo R (2006). New-generation amber united-atom force field. *Journal of Physics and Chemistry B* 110: 13166–13176.

Yang H, Yan R, Chen H, Lee DH, Zheng C (2007). Characteristics of hemicellulose, cellulose and lignin pyrolysis. *Fuel* 86: 1781-1788.

Yang CM, Hung JY, Wang YL, Lien YH (2015). Analysis of Mercedes-Benz Concept Car Using Biomimicry Design Spiral and Template Analysis–An Exploratory Study. *International Journal of Innovation in Management* 7: 49-56.

Adhityo Wicaksono

The locomotive behaviours of the tree-climbing fish, *Periophthalmus variabilis*: a cross-disciplinary approach to bioinspired design

The tree-climbing fish, *Periopthlamus variabilis* is a unique type of mudskipper that spends most of their time on the terrestrial environment. This multidisciplinary study characterized the unusual features that allows this fish to adapt for land locomotion, including tree-climbing activity using their flexible pelvic fins that facilitates mucus-induced Stefan adhesion, application of piston-like movement of pelvic fins during pectoral fins crutching movements, and water-hopping behaviour, which allows them to escape their imminent threats. From the results, the bioinspired robot design has been built as the first step of multi-phasic robot, which able to move in land and water that fills the gap in current single-phasic robotic development.

ISBN 978-952-12-4135-2